

RVSPY - Radial Velocity Survey for Planets around Young Stars

Target characterization and results from the first year of observations

Olga V. Zakhozhay^{1,2}, Ralf Launhardt¹, Andre Müller¹, Stefan S. Brems³, Trifon Trifonov¹, Martin Kürster¹, Thomas Henning¹, Sabine Reffert³, Alexey Pavlov¹, Grant M. Kennedy^{4,5}, Jayshil Patel⁶, Angela Hempel^{7,1}, Sam Kim^{8,1}, and Yashodhan Manerikar^{9,1}

¹ Max-Planck-Institut für Astronomie, Königstuhl 17, 69117 Heidelberg, Germany
e-mail: zakhozhay@mpia.de

² Main Astronomical Observatory, National Academy of Sciences of the Ukraine, 03143 Kyiv, Ukraine

³ Landessternwarte, Zentrum für Astronomie der Universität Heidelberg, Königstuhl 12, 69117 Heidelberg, Germany

⁴ Department of Physics, University of Warwick, Coventry CV4 7AL, UK

⁵ Centre for Exoplanets and Habitability, University of Warwick, Gibbet Hill Road, Coventry CV4 7AL, UK

⁶ Sardar Vallabhbhai National Institute of Technology, Surat-7, Gujarat, India

⁷ Universidad Andrés Bello, Departamento de Ciencias Fisicas, Facultad de Ciencias Exactas, Campus Casona de Las Condes, Astronomia, Fernández Concha 700, 7591538 Santiago de Chile, Chile

⁸ Astro-engineering center (AIUC), Instituto de Astrofísica, Pontificia Universidad Católica de Chile, Santiago, Chile

⁹ Indian Institute of Technology, Madras, India

Received July dd, 2020; accepted Month dd, yyyy

ABSTRACT

Context. The occurrence rate and period distribution of (giant) planets around young stars is still less well-constrained than for older main-sequence stars. This is mostly owing to the intrinsic activity-related complications and the avoidance of young stars in many large planet search programs. Yet, dynamical re-structuring processes in exoplanet systems may last significantly longer than the actual planet formation phase and may well extend long into the debris disc phase.

Aims. We search for sub-stellar companions in the planetary and brown dwarf mass regime around young stars that are surrounded by debris discs. We present the Radial Velocity Survey for Planets around Young stars (RVSPY), which is closely related to the NaCo-ISPY direct imaging survey, and aims at revealing companions at orbital separations less than a few au from the host star.

Methods. We use the FEROS spectrograph, mounted to the MPG/ESO 2.2 m telescope in Chile, to obtain high signal-to-noise spectra and time series of precise radial velocities (RV) of 113 debris disc stars with spectral types between late K and early F, a median age of 160 Myr, and at a median distance of 44 pc. Our survey is divided into two overlapping phases. During phase 1, we use short-cadence observations to characterise the intrinsic stellar activity, search for hot companions with orbital periods of up to 10 days, and derive the expected detection thresholds for longer-period (up to two years) companions. In phase 2, we continue to monitor selected targets to search for longer-period companions. In our analysis, we include archival spectroscopic, and various photometric data and use publicly available pipelines and time analysis tools (CERES, ZASPE, ATHOS, GLS, Exo-Striker).

Results. We present the results of the short-cadence observation and activity characterization of the first 70 stars. We report effective stellar temperatures (median 5900 K) and values of $v \sin(i)$ (median 7.7 km/s), derived from the FEROS spectra. For 58 stars (83%), we also derive stellar rotation periods (median 3.9 d) mostly from TESS photometry and infer inclination angles of the stellar rotation axes. We achieve a median single-measurement RV precision of 11 m/s and derive the short-term intrinsic RV scatter of our targets (median 16 m/s), which is mostly caused by stellar activity and decays with age from >100 m/s at <20 Myr to <20 m/s at >500 Myr. We find 29 stars (41%) that show clear evidence of activity-dominated variability, but no hint for the presence of a detectable short-period companion. For ten stars, we find hints for a periodic RV signal or a longer-term trend that could be related to a companion and is currently being followed-up. Six stars (9%) show large RV variability with some indication of underlying periodicity and a strong positive correlation between bisector span (a measure of line asymmetries) and RV, quite different from the anti-correlation often produced by stellar activity. We speculate that the underlying cause could be unresolved high-contrast spectroscopic companions. For 21 stars (30%), we can already exclude the presence of a massive (detectable) short-period companion. We confirm two spectroscopic binary stars and report one previously unreported 11 d spectroscopic stellar companion to HD 143811.

Conclusions. The initial short-cadence survey will be completed after about 2.5 observing years. The 2nd, long-term monitoring phase of the survey will go on for at least 2–3 more years. A statistical analysis of the entire short-cadence survey, with detection thresholds and conclusions on the occurrence rate of hot companions, will be presented in a forthcoming paper.

Key words. Methods: observational – Techniques: radial velocities – Surveys – Planets and satellites: detection – Stars: activity – Planetary systems

1. Introduction

Planets, and most likely also some brown dwarfs, are born in gaseous protoplanetary discs that surround young stars during

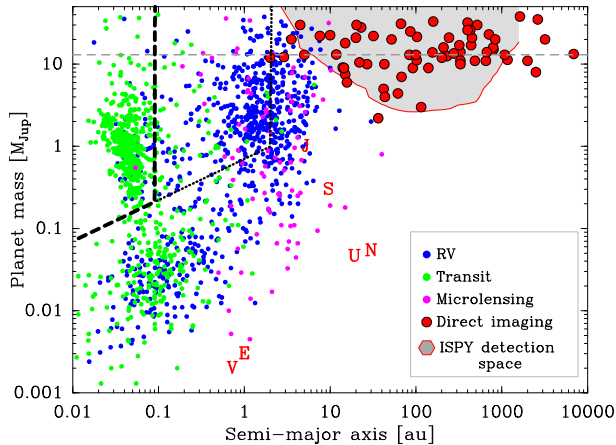


Fig. 1: Distribution of planet mass vs. orbital separation of known exoplanets and candidates as listed on exoplanet.eu (Schneider et al. 2011). The main detection methods are marked by different colours. Solar system planets are represented by red letters. The horizontal dashed line marks the approximate deuterium burning mass limit. The grey-shaded area marks the parameter space probed by NaCo-ISPY survey (10% detection probability, Launhardt et al. 2020). The thick dashed black line marks the detection space for the first year of the FEROS-RVSPY survey, assuming a mean sensitivity of 20 m/s, a maximum detectable period of 10 days, and mean stellar mass of $1 M_{\odot}$. The black dotted line shows the detection space for the anticipated follow-up observations and sensitivity to periods up to 3 yrs.

the first few million years. While we are now nearly every day gaining new insights into the structure and composition of protoplanetary discs, detections of forming protoplanets in such discs are still extremely challenging and therefore very rare (Rameau et al. 2013; Keppler et al. 2018; Müller et al. 2018).

Within only a few million years, protoplanetary discs lose their gas due to accretion onto the star and newly formed planets, but also via disc winds (Williams & Cieza 2011). By this time, the primordial dust has coagulated to pebbles and planetesimals or has been accreted onto planets. Collisional cascades within the disc then lead to the formation of debris dust. Relatively massive debris discs characterise the phase after initial planet formation when the planetary systems still evolve due to dynamical interactions and migration. By this time, the stars experience already much less chromospheric activity than at younger ages during the protoplanetary phase, such that planet searches become possible, albeit still challenging (e.g., Gregory 2017).

Several specific properties of debris discs e.g., the large inner gaps, the co-existence of hot inner dust belts, or outer dust belts that are larger than predicted by collisional cascade models, may be explained by the action of newly formed planets (e.g., Moór et al. 2015). Thus, the observable properties of debris discs could be indicative of embedded and still evolving planetary systems. Yet, the relation between debris disc properties and the existence and properties of planets has never been investigated by systematic observations of stars with debris discs. There are indications, albeit still debated, that the frequency of giant planets in young debris discs might be significantly higher than around main-sequence (MS) stars (Meshkat et al. 2017).

To systematically investigate the relation between debris disc properties and the occurrence of giant planets, the large direct Imaging Survey for Planets around Young stars (NaCo-ISPY)

was initiated in 2015 (Launhardt et al. 2020). Since direct imaging (DI) is only sensitive to companions at large separations ($>5\text{-}10$ au), we have launched a complementary systematic radial velocity (RV) survey for planets in closer orbits around these debris disc stars in 2017 using the FEROS instrument mounted at the 2.2 m MPG/ESO telescope at ESO’s La Silla Observatory in Chile (Sect. 4). Figure 1 illustrates the detection spaces of these two complementary surveys in terms of planet masses and semi-major axes.

This paper introduces our systematic RV survey for giant planets and brown dwarfs around young stars (RVSPY) with debris discs in orbits shorter than seen by direct imaging. The paper is organised as follows: In Section 2 we outline the motivation, goals, and general survey strategy. The targets are presented in Section 3, the observations and data reduction as well as analysis are described in Sections 4 and 5 (respectively). Results from the first year of observations are presented in Section 6 and discussed in Section 7. Section 8 summarises the paper.

2. Motivation, goals and survey strategy

The main goal of the RVSPY survey is to constrain the occurrence rate of Jovian-mass planets around young low- and intermediate-mass stars during their debris disc phase. We aim to investigate the relation between the occurrence of such planets and the properties of the debris discs, which will provide important constraints for informing planet formation and evolution models that are used in planet population synthesis modelling.

Different planet detection methods have different detection biases and each method alone can explore only a certain part of the parameter space we are interested in. While DI is only sensitive to planets with large enough projected angular separations to be spatially resolved from the bright host star, RV has the opposite detection bias, i.e., it is most sensitive to planets orbiting their host stars at small separations and with short orbital periods (Fig. 1). Thus, combining these two methods by designing this FEROS-RVSPY survey such that it has the largest possible target overlap with the NaCo-ISPY DI survey (Launhardt et al. 2020) will allow us to characterise the (giant) planet population around young debris disc stars over most orbital scales.

However, the two methods do not harmonize easily in all aspects. DI works best for young stars, when the planets are still hot from the formation process, and thus bright. Young stars in general rotate fast and the interplay between stellar rotation, convection, and magnetic fields, in particular in cool stars, leads to enhanced photospheric (e.g., star spots) and chromospheric (e.g., emission lines) activity. Both can alter the effective shape of spectral lines such that rotational modulation of line shapes due to activity features in the stellar atmosphere leads to an effective jitter (random or quasi-periodic) of the measured mean RV which can mask or even mimic the RV modulation caused by an orbiting (planetary) companion (Hatzes 2002). This magnetic activity decays with the slowing down of the stellar rotation due to wind braking on time scales of 100 Myr (at $1 M_{\odot}$) to Gyr (at $<0.3 M_{\odot}$; Bouvier et al. 2014).

Stars less massive than approximately $1.3 M_{\odot}$ and cooler than $T_{\text{eff}} \approx 6500$ K (corresponding to a main-sequence spectral type later than F5) maintain a convective envelope in which dynamo processes generate a permanent magnetic field that causes the stars to spin down via magnetic braking as they evolve. Consequently, such stars, when sufficiently slowed down, usually have many (because they are cool) and narrow (because they rotate slowly) absorption lines in their spectra and are thus well-suited for precision RV measurements. In stars more massive

than about $1.3 M_{\odot}$, the dominating energy-efficient CNO cycle leads to the formation of a convective core and a radiation-dominated envelope in which no efficient dynamo can generate magnetic fields which could slow down the stellar rotation. These stars have not only fewer (because they are hotter), but also much broader spectral lines and are therefore less suited for precision RV measurements.

Hence, RV planet searches around young stars require a careful consideration of stellar ages, rotation velocity indicators (e.g., $v \sin(i)$), and stellar spectral types (T_{eff}) when defining the target sample and tailoring the observing strategy and cadence of the RV measurements. An efficient synergy between DI and RV planet searches is most promising for stars older than about 10 Myr, but not older than a few hundred Myr, and for spectral types of F5 or later. Attention should be given to pre-main-sequence (PMS) stars younger than about 50 Myr, which are still contracting and heating up and may still rotate relatively fast even if their mass is below $1.3 M_{\odot}$. With these considerations we define our target selection criteria by drawing a suitable sub-sample from the ISPY target list, and extend it with more debris disc targets that were not observed within ISPY (Sect. 3).

As outlined above, the target stars in question still exhibit stronger stellar activity than their more evolved MS counterparts. Rotational modulation of spectral line strengths and shapes due to activity-related stellar surface features causes signals that interfere with precise RV measurements. Therefore, it is mandatory to characterise the intrinsic stellar activity on the rotational time scales before attempting to search for RV variations that could be caused by orbiting companions. Rotational periods of young low- and intermediate-mass stars are well-explored and are typically constrained to periods between 1 and 10 days with a bimodal distribution peaking at ~ 8 days (slow rotators) and ~ 2 days (fast rotators; e.g., Herbst et al. 2002). The orbital period distribution of 'hot Jupiters', which are thought to have formed at larger separations in the discs and migrated inwards (e.g. Lin & Papaloizou 1986; Dawson & Johnson 2018), peaks in a similar range at 3–5 days.

Hence, with high-cadence RV measurement series covering about two weeks, with one to three spectra per night, we can both characterise the most significant activity-related variability of our targets as well as constrain the presence of hot companions (HC, which include hot Jupiters). Although HC seem to be rare around "normal" MS stars (Wright et al. 2012), this may not necessarily apply to the stars with massive debris discs. Since HCs induce much larger RV signals than longer-period planets, they are also easily detectable in Doppler data. Therefore, the initial phase of our FEROS-RVSPY survey is tailored to sample variability time scales of $\sim 1 - 10$ days to characterise stellar activity, while at the same time screening for the presence of HC. The results and detection thresholds derived from this initial high-cadence survey are then used to identify those targets for which searching for longer-period companions (months up to 2–3 yrs) seems feasible. In the second phase of the RV survey, we continue to monitor the stars from this down-selected sample with an adapted lower cadence for up to a few years.

3. Targets

3.1. Target selection criteria

In accordance with our science goals and the specific complications outlined in Sect. 2, we restrict our target list to stars with a confirmed debris disc signature and with ages of ≥ 10 Myr. The latter is done to avoid the most active phase of young

stars and the overlap to the preceding protoplanetary disc phase (see Fig. 6 in Launhardt et al. 2020). It has been shown by Brems et al. (2019) that the mean activity-induced RV jitter of young solar-type stars decreases from $\gtrsim 500$ m/s at 5 Myr to $\lesssim 200$ m/s at 10 Myr, thus making age a crucial parameter for the target selection. Spectral types are restricted to the range F6–M2, because earlier types have too broad and too few spectral lines (see Sect. 2), and later spectral types have too many spectral lines that blend. Furthermore, they are known to have less massive debris discs and fewer giant planets. We also set a brightness limit at $V \leq 10.5$ mag to limit individual exposure times. The declination range is naturally set to $-75^{\circ} \leq \text{DEC} \leq +25^{\circ}$ by the location of the La Silla observatory. For some particularly interesting targets, the limits on declination and spectral type were not strictly obeyed. In particular we included a few stars with earlier spectral types (up to A7) to verify their $v \sin(i)$ and the achievable RV precision from test spectra before a decision was made to schedule them for high-cadence RV monitoring.

We also did not include stars for which a sufficiently large number of useable RV data was already available in archives. For this purpose we have queried the ESO archive (FEROS, HAPRS¹) and the Keck archive (HIRES²). Stars with less than ten archival spectra are still kept in our survey list. Stars with ≥ 120 spectra are excluded, but we will analyse their archival data in the same way as our own FEROS spectra and include the results in our final survey analysis (see below). For stars with an intermediate number of archival spectra, we verified case by case whether sequences of spectra with sufficiently high cadence (see Sect. 4.1) were available and included or rejected them from our survey list.

Also in accordance with our main science goals, we selected our core target list for this RV survey from the target list of the NACO-ISPY survey (Launhardt et al. 2020), with the RV-specific selection criteria described above. This resulted in a list of 54 targets. However, for statistical reasons, in order to put robust constraints on the frequency of giant planets in debris discs and their relation to debris disc properties, one would ideally have a total sample size of ≥ 200 stars. We therefore enlarged our core target list by 59 additional targets selected from the *Spitzer* IRS catalogue of Chen et al. (2014), and from Cotten & Song (2016) based on the shape of the IR-excess and the location of the stars in the Hertzsprung–Russell diagram. Some of these stars were actually already included in the NACO-ISPY master target list, but could not be imaged in the end. Finally, our target list for the final statistical analysis will be complemented by those stars that match our selection criteria and for which we could already obtain ≥ 120 useable archive spectra. These additional targets are not included in the survey target list we describe in this paper.

We verified the significance of the disk IR excess emission (see below) only after the survey observations had started, and 19 stars selected from Chen et al. (2014) and Cotten & Song (2016) turned out to show marginal or no debris disk emission³. These 19 stars will neither be scheduled for longer-term monitoring (Sect. 4.1), nor will we use them for our anticipated statistical analysis of the occurrence rate of GPs around debris disc stars.

¹ HAPRS – High Accuracy Radial velocity Planet Searcher, mounted at 3.6 m telescope at La Silla observatory in Chile (Mayor et al. 2003).

² HIRES – High Resolution Echelle Spectrometer, mounted on the 10 m Keck I telescope, USA, Hawaii (Vogt et al. 1994).

³ For most of these 19 stars the issue appears to be related to normalisation of *Spitzer* IRS spectra as discussed by Kennedy & Wyatt (2014) (their Sect 4.3).

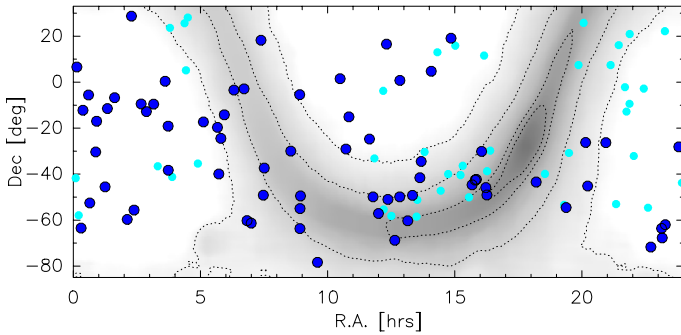


Fig. 2: Sky distribution of all 113 targets of this survey; observed in high cadence (dark blue) and not yet observed (light blue). The grey-shaded area and dotted contours outline the Milky Way disc and bulge as traced by the COBE-DIRBE band 2 (K) zodi-subtracted all-sky map (Hauser et al. 1989).

3.2. Target properties

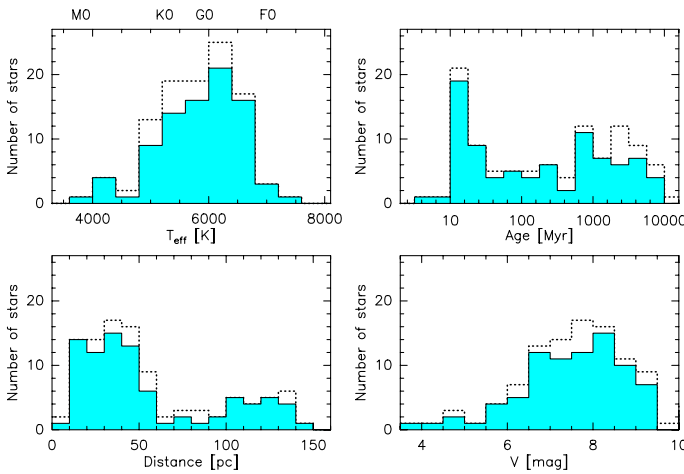


Fig. 3: Histograms showing the distribution of stellar effective temperatures, ages, distances, and V magnitudes of our survey targets. Dotted histograms show all targets, while the blue filled histograms account only for targets with confirmed debris disc signal (see Sect. 3).

Our final target list for the survey observations consists of 113 stars, of which 54 stars were also imaged with NACO and 19 out of the additional 59 targets turned out to not have significant debris disc excess. The targets are evenly distributed over the sky (Fig. 2).

Basic stellar parameters as well as the disc IR excess are compiled from different sources to select and characterise our targets. Spectral types and V magnitudes are compiled from the Hipparcos and Tycho Catalogues (van Leeuwen 2010; Høg et al. 2000) and from the SIMBAD database. Distances were inferred from *Gaia* DR2 parallaxes (Gaia Collaboration et al. 2016, 2018) with the method described by Bailer-Jones et al. (2018).

Stellar luminosities, L_* , effective temperatures T_{eff} , radii R_* , and disc parameters, T_{dust} , R_{BB} , and L_{disc}/L_* , are derived by fitting stellar (PHOENIX; Husser et al. 2013) and blackbody models to observed photometry and spectra simultaneously (for more details see Yelverton et al. 2019, 2020; Launhardt et al. 2020). The photometry is obtained from multiple catalogues and publications, including 2MASS, APASS, Hipparcos/Tycho-2, Gaia,

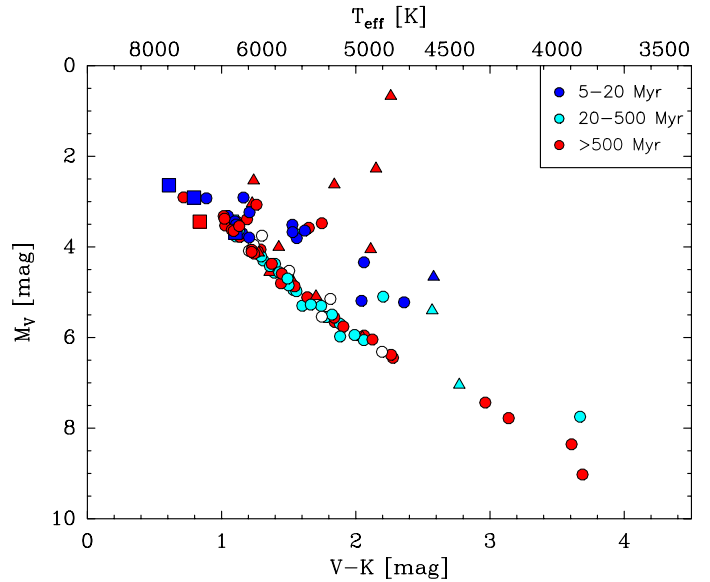


Fig. 4: Colour-magnitude diagram of RVSPY targets. Marked on top are the effective temperatures which a main-sequence star with the corresponding $V - K$ colour would have (Cox 2000). Stellar ages are colour-coded: dark blue: 5–20 Myr, light blue: 20–500 Myr, red: >500 Myr, empty: age not known. Stars marked as triangles do not have significant IR excess (see Sect. 3.1). Stars marked as squares show a significant positive correlation between RV and bisector span ($r_P > 0.7$, see Sect. 6.2).

AKARI, WISE, IRAS, Spitzer, Herschel, JCMT, and ALMA. In some cases, photometry has been excluded, for example due to saturation or confusion with background or other objects.

In this initial stage of our survey, we do not use the actual disc parameters yet⁴, but only evaluate the significance of the disc excess to select the targets. Stellar effective temperatures derived this way were used for initial target selection, but are later replaced by values derived via flux ratio pairs obtained from FEROS spectra with the ATHOS pipeline (Hanke et al. 2018). Values of $v \sin(i)$ are derived from FEROS spectra using the open source ZASPE pipeline (Brahm et al. 2017b). Since the derivation of uncertainties for individual stars is computationally very expensive, we computed them only for selected cases with $v \sin(i)$ coming closest to 3, 5, 10, 20, 30, 40, and 50 km s^{-1} . Based on the computed uncertainties for these example cases we derive an empirical fit of the form $\sigma_{v \sin(i)} = \sqrt{v \sin(i)}$, with a lower limit of 5% towards larger $v \sin(i)$, for all our targets, with the following exception. For values of $v \sin(i) < 3 \text{ km s}^{-1}$, we can no longer distinguish between instrumental and rotational broadening of the spectral lines and adopt therefore a lower limit of 3 km/s (Reiners et al. 2012).

Ages are compiled from the literature and therefore derived with different methods and different treatment of uncertainties. Target list parameter distributions are shown in Fig. 3. Figure 4 shows the colour-magnitude diagram of our target stars with the stellar ages colour-coded. The main sequence is clearly visible. It is also evident that all the very overluminous stars are actually old stars (giants) without significant IR debris disc excess, that were erroneously included in our initial target list, but will not be followed-up further (see Sect. 3.1). There is also a number of only slightly overluminous stars that are younger than 20 Myr

⁴ The results of spectral energy distribution modelling and analysis will be presented in a future paper.

and have significant IR excess from debris discs. These are still pre-main sequence stars.

Target names, coordinates, and most physical parameters mentioned above of those 70 stars observed during the first survey year, including individual age references, are listed in Table 2.

4. Observations

4.1. Observing strategy

As outlined in Sect. 2, the first phase of our survey is designed to characterise the stellar activity jitter of all targets on the timescales of their rotational periods (that will help to identify the activity induced signals), and to search for HCs. For this purpose, we schedule every target star for one period of high-cadence observations consisting of 14–15 consecutive nights in which we obtain one spectrum per night and star during at least 13, ideally consecutive nights, plus 2–3 spectra per night during one to two nights. The order in which the stars during one such block are observed is changed from night to night and within their visibility time to avoid exact 24 hr window function peaks in the periodograms, thereby probing the frequencies/periodicities relevant for both activity-related rotational modulation and hot companions.

Since the more quiet stars in our sample exhibit an RV scatter of order 10 m/s (see Fig. 11), we aim for an intrinsic RV precision of $\sigma_{RV} \leq 50$ m/s, which we typically achieve with an $S/N \gtrsim 100$, although the RV precision also depends on the stellar spectral type, atmospheric condition, etc.. A detection limit of 50 m/s corresponds to the RV amplitude induced by a $1 M_{Jup}$ -mass planet in a 3-d orbit around a solar-mass star. In addition to the high-cadence observations, we take individual "test" spectra for stars that did not have any archival spectra available to assess their basic stellar parameters and the achievable RV precision (Sect. 3.2) and to decide whether or not they will be scheduled for high-cadence observations.

The results and detection thresholds derived from this initial high-cadence survey are then used to identify those targets for which searching for longer-period companions (months up to 2–3 yrs) seems feasible. In the second phase of the survey, we will continue to monitor the stars from this down-selected sample with an individually adapted lower cadence for up to a few years (see Sect. 7).

During the second observing semester, we already complement the high-cadence observations of the remaining survey targets with lower-cadence follow-up monitoring of a sub-sample down-selected based on the results from the high-cadence survey in the first semester.

4.2. High-cadence observations

During the first four observing campaigns of this survey, between April 2018 and March 2019 (see Table 1), we obtained high-cadence time series of spectra for 70 out of our 113 survey targets. The observing campaigns typically consist of about 14–15 consecutive nights.

All observations are carried out with the FEROS instrument, a Fiber-fed Extended Range Optical Spectrograph, mounted at the 2.2 m MPG/ESO telescope at ESO's La Silla Observatory in Chile (Kaufer et al. 1999). FEROS provides a spectral resolution of $R = 48000$, high efficiency ($\sim 20\%$), and covers the wavelength range 350–920 nm. All spectra are taken in the "object calibration" mode of FEROS with one fiber on the star

and the second fiber observing simultaneously the "ThAr+Ne" calibration lamp. Standard calibration files (BIAS, FLATS, and lamp spectra for wavelength calibration 'WAVE') are taken before each observing night during the afternoon and reduced with the CERES pipeline (see Sect. 5.1 for details). To monitor the long-term stability of the spectrograph, we also observe a few RV standard stars during each campaign.

The required $S/N \geq 100$ (Sect. 4.1) is achieved with integration times between 6 min for stars with $V \leq 6$ mag and 20 min for stars with $V = 10 - 11$ mag. When the seeing exceeded 1.8'', the exposure time was increased. To ensure that the required S/N is actually achieved, and to identify possible spectroscopic binaries early on, we verify the data quality during the observations and analyse the RV time series after the first few observing nights of each run. The weather was good during most of the nights, with clear to thin cloud conditions and seeing mostly in the range 0.6'' – 1.7'' (median 1''). No observations were taken when the seeing exceeds 2.5''. About 10% of time was lost due to bad weather conditions (thick clouds or strong wind). Table 1 summarises the observing campaigns.

4.3. Complementary data

To extend the temporal baseline of the RV data of our targets, we look for available archival spectra or already processed RVs that qualify for our purpose and can be combined with our own FEROS data. Archival FEROS spectra, which were not taken during our program, were downloaded from the RAW ESO Science Archive⁵ and reduced and analysed with the same procedure as we use for our own observing data.

For 21 targets, we find precise Keck/HIRES RV data in the HIRES archive published in Tal-Or et al. (2019)⁶. In addition, we find precise HARPS RV data and activity indicators for 38 targets in the HARPS-RVBANK⁷ (Trifonov et al. 2020).

Following Trifonov et al. (2020), RVs and activity indicators derived from HARPS spectra taken before and after the fiber-upgrade in May 2015 (Lo Curto et al. 2015) are treated as separate data sets because of the notable RV offset induced by the hardware intervention. Table 3 summarizes all the archival spectra we have used for the analysis.

Furthermore, we use photometric time series data to derive additional constraints on stellar rotation periods and activity cycles. The majority of our targets (88%) are in the TESS⁸ observing list. For 56 of the 70 targets presented in this paper, the TESS data are already publicly available, retrieved, and included in our analysis (Sect. 6.3).

5. Data reduction and analysis

5.1. Tools

The basic reduction of the spectra and the extraction of RVs are done in a semi-automatic fashion with the CERES pipeline (Brahm et al. 2017a). CERES computes the RV of an observed spectrum by cross-correlating it with a binary mask for the stellar spectral lines. CERES provides three default masks for spectral types G2, K5, and M2. We use the mask that comes closest to the spectral type of a star (Table 2).

⁵ http://archive.eso.org/eso/eso_archive_main.html

⁶ Originally, this is the HIRES archive published by Butler et al. (2017), but corrected by Tal-Or et al. (2019) for small systematic errors in the RVs.

⁷ www.mpa.de/~trifonov/HARPS_RVBANK.html

⁸ TESS – Transiting Exoplanet Survey Satellite (Ricker et al. 2015a).

Table 1: Observing campaigns

Dates	ESO Period / Run ID	Nights ^a	Time ^b	Stars (spectra) ^c
2018, Apr 16 – 30	101 / 0101.A-9012(A)	14	65h47m	19 (307)
2018, Jul 30 – Aug 16	101 / 0101.A-9012(B)	15	76h12m	22 (372)
2018, Nov 30 – Dec 13	102 / 0102.A-9008(A)	15	54h32m	15 (301)
2019, Feb 13 - 27 ^d	102 / 0102.A-9008(B)	14	66h10m	14 (334)

Notes. ^(a) Number of nights with more than one useful spectrum. ^(b) Total exposure time dedicated to the program during the observing run. ^(c) Number of stars for which high-cadence time series were obtained and total number of spectra taken during the run. ^(d) Due to interruptions by directors discretionary time (DDT) and target of opportunity observations (ToO), some extra compensation time was scheduled during March 22–31, 2019.

The shape of the resulting cross-correlation function (CCF), which is also provided by CERES, is an important carrier of information about the origin of the measured RV variations (see below). For the computation of periodograms from time series data of RVs and various other quantities, we use the Generalized Lomb-Scargle (GLS) periodogram tool by Zechmeister & Kürster (2009), with the eccentricity fixed to zero and sine frequency/period output. For the extraction of stellar parameters, we use the ZASPE (Brahm et al. 2017b) and ATHOS (Hanke et al. 2018) pipelines. To fit the RV data and derive the orbital parameters of the hypothetical companions we used The Exo-Striker fitting toolbox (Trifonov 2019).

5.2. Activity indicators

Stars generally exhibit higher levels of activity when they are young as compared to the rather quiet stage on the main sequence (e.g. Gregory 2017; Brems et al. 2019). Hence, possible planet signals in the RVs will always be accompanied by some degree of activity-related rotational modulation of the spectra, such that planet signals do not stand out as clearly. Their recovery requires, besides an adapted observing strategy (Sect. 4.1), both a special analysis strategy and a case-by-case treatment. These difficulties are also reflected in the unofficial sub-title of our initial RVSPY survey, “*Hot planets and rubble - let’s face the trouble*”.

Rotational modulation of spectral line shapes due to activity features on the stellar surface can induce large RV scatter that can mask a planetary RV signal or even mimic it, when the spots are stable. To characterise the stellar activity and disentangle possible planetary signals from activity-induced RV variations, we derive the following activity-related parameters and calculate the following metrics for all our observed spectra:

- equivalent widths (EWs) of H α , H β , and H γ ,
- H α line index according to the definition by Kürster et al. (2003), but with an adapted wavelength range provided by Boisse et al. (2009),
- Ca II H&K S_{index} according to the definition by Duncan et al. (1991)
- line profile variance of Ca II H&K, H α , H β , and H γ as defined in Johns & Basri (1995), to identify and quantify line variability,
- line depth ratios of temperature-sensitive lines using line pairs as defined in Biazzo et al. (2007),
- bisector shape, span (BS), displacement, and curvature as defined in Povich et al. (2001),
- full width at half maximum (FWHM) of the cross-correlation function derived by CERES,
- time series of photometric data from TESS (Ricker et al. 2015b), from which we derive stellar rotation periods, P_{rot} , as described below.

To distinguish periodic RV variations caused by a physical companion from those that are related to rotational modulation of line shapes, we calculate both GLS periodograms and linear correlations of all activity indicators with the RVs. In addition, to detect periodic variations of the line profiles or small parts of the lines, we calculate two-dimensional GLS periodograms for the Ca II H&K, H α , H β , and H γ lines (see Fig. A.4).

Depending on spectral type and age of the star, as well as geometrical aspects, chromospheric and photospheric activity can occur at different levels and might not be detectable equally in all indicators. For example, a well-established indicator to identify periodic rotational modulations of line shapes by dark spots on the stellar surface is the correlation between bisector span (BS) and RV. A strong anti-correlation between BS and RV is a clear indication of a dark spot (e.g. Queloz et al. 2001). However, depending on the inclination of the star, the spot latitude, and $v \sin(i)$, the strength of the correlation and the amplitude of the BS can vary significantly (e.g. Desort et al. 2007). It is therefore necessary to rely not only on one indicator, but to measure a variety of indicators of different origin and different sensitivities, especially in the case of a large RV survey. In Appendix A, we demonstrate exemplarily our described activity analysis for one star in our sample, HD 38949, for which most activity indicators show clear and unambiguous signals.

In addition, we use GLS periodograms of the photometric time series data from TESS (Sect. 4.3), where available, to independently derive stellar rotational periods (Sect. 6.3). Knowing the stellar rotation period not only helps us to derive the inclination of the stellar spin axis (Sect. 6.3), but also helps to interpret RV periodograms and to distinguish rotational modulation from companion-related RV variability (Sect. 6.2).

6. Results from the first year of observations

By the end of the first two observing semesters, we have obtained high-cadence time series of spectra for 70 stars. In addition, we took 46 individual test spectra for stars that did not have any previously observed FEROS or HARPS spectra available in the ESO archive. In total, we have obtained 1 314 individual spectra with a total integration time of ≈ 263 hrs. Figure 2 shows the distribution of our targets on the sky. Target names, coordinates, and main physical parameters of the 70 survey stars presented in this paper are listed in Table 2. All spectra are reduced using the CERES pipeline (Brahm et al. 2017a) with default settings. Initial inspection of the RV series showed that at least 20% of the targets require follow-up observations to verify signal candidates identified in the short-cadence observations or to search for possible longer-period companions. For a few targets, the first follow-up observations are already taken during the second observing semester.

6.1. Basic stellar parameters

Basic stellar parameters T_{eff} , L_* , R_* , and $v \sin(i)$ are derived from the FEROS spectra and the compiled photometry as explained in Sect. 3.2. In Table 2 we report the results on T_{eff} , L_* , and $v \sin(i)$. The stellar radii are used to compute the equatorial rotation velocities of the stars (Sect. 6.3). The spectroscopically derived values of T_{eff} agree very well (within the uncertainties) with the photometrically derived values reported in Launhardt et al. (2020). Figure 3 shows the distribution of T_{eff} for our targets, which ranges from ≈ 4000 K (K7) to ≈ 7000 K (F0), and has a median value of ≈ 5900 K (G0). Bolometric stellar luminosities range from ≈ 0.1 to $\approx 13 L_\odot$, with a median value of $\approx 1.7 L_\odot$. Values of $v \sin(i)$ range from < 3 km/s (see Sect. 3.2) to ≈ 90 km/s, with a median value of ≈ 7.7 km/s. Figure 10 (Sect. 7.3) shows the distribution of $v \sin(i)$ values vs. age and T_{eff} . Other basic stellar parameters listed in Tab. 2, such as V magnitudes, spectral types, and stellar ages, are compiled from the literature.

6.2. Radial velocity variability and bisector dependence

To quantify the RV variability of our targets on a 2-week time scale, we first look at the intrinsic rms scatter of the RVs, irrespective of whether there are periodicities in the RVs or not. We achieve a median single-measurement RV precision of $\langle \sigma RV \rangle = 11$ m/s (mean 44 m/s), and measure a median short-term intrinsic RV scatter, $rms_{\text{RV}}(\tau 14\text{ d}) = \sqrt{rms_{\text{obs}}^2 - \sigma RV^2}$, of 16 m/s (mean 126 m/s, excluding spectroscopic binary stars). Figure 5 shows rms_{RV} vs. the effective temperature, T_{eff} , for all targets. Apart from the three spectroscopic binaries (see below), we observe RV rms scatter values between 3 and 1600 m/s, with a general trend of scatter increasing with T_{eff} . The three spectroscopic binaries all have $rms_{\text{RV}} > 4$ km/s. There are two groups of apparent outliers visible in Fig. 5, which we describe and discuss in more detail below. Four stars with T_{eff} between 3900 K and 5500 K have rms_{RV} scatter between 70 m/s and 400 m/s, higher than the bulk of the other targets that are all very clearly dominated by rotational modulation due to star spots. Another group with $T_{\text{eff}} > 6400$ K and $rms_{\text{RV}} > 400$ m/s is discussed below.

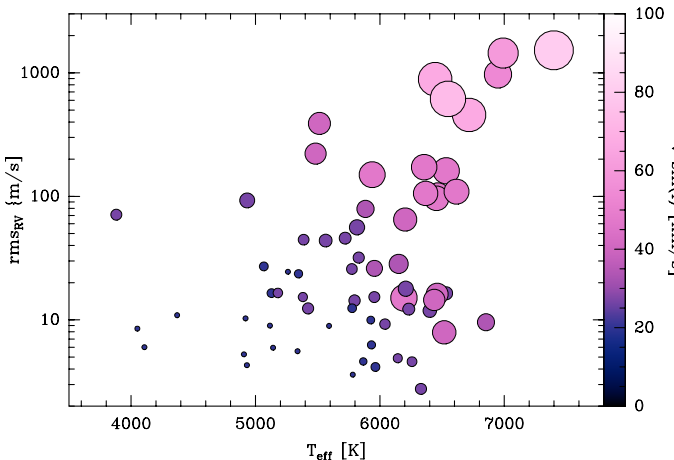


Fig. 5: Intrinsic rms scatter of the RVs in the 2-week high-cadence data vs. effective stellar temperature, T_{eff} , with $v \sin(i)$ encoded in marker size and color. The three spectroscopic binaries are outside the plotting range for rms_{RV} .

To further evaluate the nature of the RV variability, we analyse the time series periodograms⁹, the correlation between BS and RV (Queloz et al. 2001), and the shape of the cross correlation functions (CCF), and divide the 70 stars with high-cadence time series of spectra into five main categories:

1. Stars that show clear evidence of activity-dominated variability,
2. Stars which show a positive correlation between BS and RV (see below),
3. Stars with (to be confirmed) companion candidates,
4. Stars with inconclusive RV modulation,
5. Spectroscopic binary stars.

1) For 29 of the 70 stars (41%), we measure a moderate ($-0.5 > r_P > -0.7$)¹⁰ to strong ($r_P \leq -0.7$) anti-correlation between BS and RV, indicating that stellar spots dominate the observed RV variation (Fig. 8). All of these activity-dominated stars have $5000 \text{ K} < T_{\text{eff}} < 6500 \text{ K}$, i.e., spectral types between K2 and F5, and $v \sin(i) < 40$ km/s (Fig. 8). The strength of the correlation and the amplitude of the BS variation depends on the star-spot geometry: the inclination of the star, the spot latitude, $v \sin(i)$ (Desort et al. 2007), and on the inhomogeneity (asymmetry) of the spot distribution. To fully understand the cause of the observed RV variations (companion vs. stellar activity), we compute and analyse a number of activity indicators (Sect. 5.1) and incorporate photometric data, where available (Sect. 6.3). An example of this approach is described in more detail in App. A for HD 38949. The majority of these 29 activity-dominated stars show (mostly non-significant) RV variability with the same period as the respective photometric variability (Sect. 6.3), which further hints at rotational modulation due to star spots. For none of these 29 active stars we find significant evidence for additional periodic RV variability that could indicate the presence of a HC.

A few more stars with less significant anti-correlation between BS and RV show RV periodicity that coincides with a significant signal in the TESS photometry periodogram at a period that is typical for rotational modulation (≈ 1 – 20 d, Sect. 6.3). The clearest example of these is CPD –72 2713, which we show in App. B.

2) Six stars (9%) show a strong positive correlation between RV and BS ($r_P > 0.7$), which cannot be caused by star spots, because any local brightness changes on the surface of the star (dark or bright spots) will cause such CCF deformations that there is an anti-correlation between RV and BS. Three more stars with only moderate correlation ($0.5 < r_P < 0.7$) are not further considered here because they have fewer data points and the correlation is therefore not trustworthy. The underlying physical cause of a positive correlation between BS and RV is poorly understood. We discuss it in more detail in Sect. 7.1.

3) 35 stars (50%) do not show a significant correlation between BS and RV on the monitored two-week time scale ($-0.5 < r_P < 0.7$). For ten of these, we see (not yet significant) hints for a periodic RV signal at short periods ($P < 14$ d), or a longer-term trend that is not correlated or anti-correlated with the BS and does not coincide with a photometric period from TESS or the literature. These targets are scheduled for follow-up monitoring because additional data and longer time baselines are required to prove or disprove the presence of companions around them.

4) Four of the 35 stars without significant BS(RV) correlation show some correlation between photometric and RV variability,

⁹ We use the Generalized Lomb-Scargle (GLS) periodogram tool by Zechmeister & Kürster (2009), with the eccentricity fixed to zero.

¹⁰ r_P = Pearson correlation coefficient

hinting at spot-related rotation modulation. 21 stars show inconclusive (non-periodic) RV modulation with the majority having an rms scatter of $r_{\text{RV}} < 100 \text{ m/s}$, but extremes ranging from 5 m/s to 980 m/s. For these stars we can basically exclude the presence of a massive HC, but we evaluate on a case-by-case if they are suited for follow-up monitoring to search for longer-period companions (Sect. 7.5).

5) Three stars, all without significant correlation between RV and BS, turned out to be spectroscopic binaries. HD 16673 (Gorynya & Tokovinin 2018) and HD 141521 (Weise et al. 2010) were actually known before, but this information was overlooked in our selection process. With HD 143811 we discovered a previously unreported binary. HD 143811 is a young, 11 Myr old F5 V star (Chen et al. 2014). It was observed during the first RVSPY observing campaign in April 2018. The cross correlation function (CCF) clearly reveals the star as a double-lined spectroscopic binary (SB2) with a period of ≈ 11 days. Since the CERES pipeline does not allow us to derive precise RV for individual components of the binary system and hence we can not derive reliable orbital parameters yet, we will provide more details in a forthcoming paper.

6.3. Stellar rotation periods and inclinations

We use GLS periodograms (Sect. 5.1) of the TESS light curves where available (Sect. 4.3) to infer stellar rotation periods of our targets. Since any brightness inhomogeneities on the stellar surface, such as star spots or dominant groups of spots, will cause a periodic rotational modulation of the light curve, the stellar rotation periods should be visible in periodograms of photometric time series data with appropriate sampling and time coverage. The TESS light curves cover a time interval of about 27 days (cadence ≈ 2 min), which is comparable to the time span of our high-cadence RV observations and covers the range of rotation periods expected for our targets (see Sect. 2). The TESS data should thus be well-suited to independently identify the stellar rotation periods.

In fact, in the absence of massive HCs (Sect. 7.4), star spots should dominate the photometric variability of most of our stars that are young and usually active in a similar way as they dominate the RV variability¹¹ (Sect. 7.4 and Fig. 11). This is nicely demonstrated by Fig. 6, where we show the relative intrinsic rms scatter of the high-cadence RV data, inversely scaled with $v \sin(i)$, vs. the rms scatter of the photometric TESS data (cleaned from outliers and obvious flares) for those 56 targets for which the TESS data are available. Apart from the three spectroscopic binaries and a few other outliers, which we discuss in Sect. 7.1, there is a relatively tight correlation between the photometric and RV scatter on a two-week timescale, as one would expect from spot-dominated rotational modulation. This is supported by the fact that nearly all stars with relative photometric rms scatter > 0.001 exhibit a significant anti-correlation between RV and BS (Fig. 6), as one would expect from spot-dominated rotational modulation of the RVs.

For 37 of the 56 targets with TESS data, we could clearly identify a single dominant period as P_{rot} . To verify if this is indeed a physically meaningful rotation period, we evaluate for every star if the resulting equatorial rotation velocity $v_{\text{eq}} = 2\pi R_*/P_{\text{rot}}$ is larger than the measured $v \sin(i)$. Indeed, this

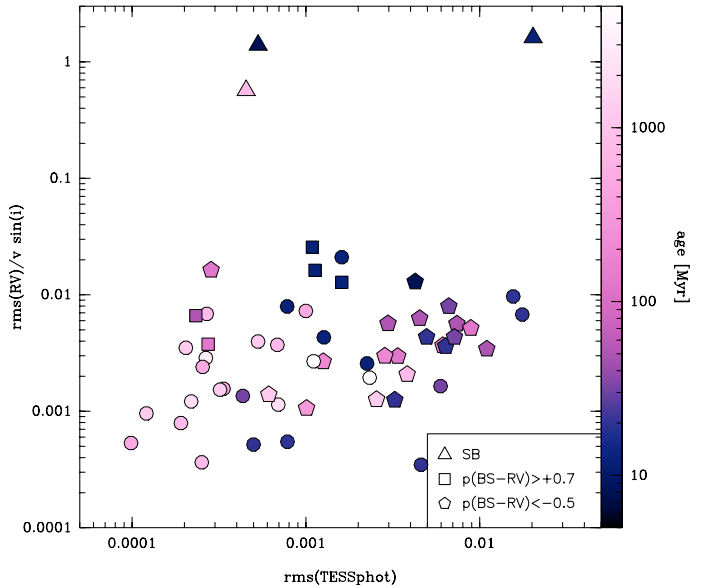


Fig. 6: Relation between short-term ($\tau=14$ d) photometric (TESS) and relative intrinsic RV scatter, inversely scaled with $v \sin(i)$, for all targets with TESS photometry. Ages are color-coded. Triangles show spectroscopic binary stars, pentagons mark stars with a significant anti-correlation ($r_P < -0.5$) between RV and BS, indicating strong spot activity (Sect. 6.2), and squares mark targets with a strong positive correlation ($r_P > 0.7$) between RV and BS, which we discuss in Sect. 7.1.

is the case for all 37 stars. We consider the rotation periods for these 37 stars as secure.

For 20 stars, we could derive likely rotation periods with different degrees of uncertainty, ranging from larger error bars to possibly having selected the wrong period. Since young stars may have more than one dominant spot or spot group, there could be more than one significant spot-related period evident in the periodograms. Indeed, we find $\approx 2:1$ period pairs in the TESS periodograms of eleven of our targets. In these cases, the longer of the two periods is more likely to be the stellar rotation period, and the shorter period should reflect a second dominant spot (group). While this works out well for 8 of the 11 stars, only the shorter of the two periods is physically possible for three stars according to the $v \sin(i)$ test. For two stars (HD 15060 and HD 101259), we identify a dominant, albeit not statistically significant period that was in the physically possible range for being the rotation period. For two other stars (HD 76748 and CD-49 3972), we identify a significant periodogram power over a narrow range of periods, but no single dominant period. Here, we adopted the mean period as P_{rot} , with a correspondingly large uncertainty interval.

For two stars without TESS data, but with strong anti-correlation between RV and BS (see Sect. 6.2; HD 33081 and HD 107146), we identify a marginally significant period in our RV data, which we interpret as the most likely rotation period. For two stars (HD 111520 and HD 115820), the most significant period is too long to be the stellar rotation period (according to the $v \sin(i)$ test), and we adopted a less significant shorter period as P_{rot} . One of these (HD 115820) turns out to be a δ Scuti variable (Bedding et al. 2020), with pulsation modes in the frequency range $20-35 \text{ d}^{-1}$. Finally, for two stars without TESS data (HD 90905 and HD 191089), we find otherwise photometrically derived, but only tentative rotation periods in the literature.

¹¹ δ Scuti variable stars (sometimes termed dwarf cepheids) can have pulsation periods of the order of hours, i.e., shorter what we expect to be the rotation periods of our targets. However, there might be cases where the ranges overlap (if the target happens to be a δ Scuti variable).

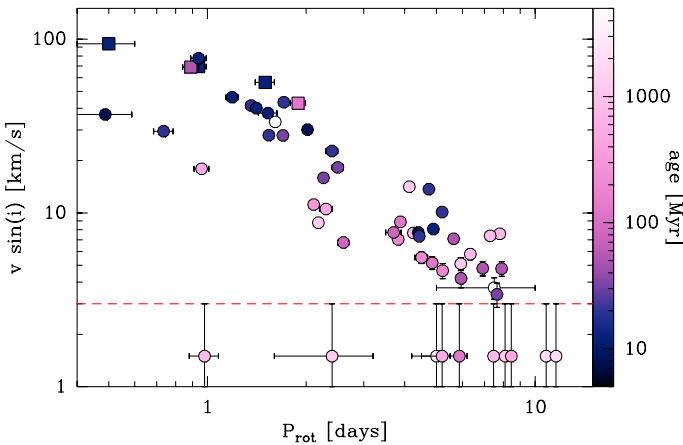


Fig. 7: Rotational line broadening, $v \sin(i)$, as derived from FEROS spectra, vs. stellar rotation periods derived from TESS light curves. Ages are color-coded. Squares mark targets with a strong positive correlation ($r_P > 0.7$) between BS and RV. The horizontal dashed red line marks the lower sensitivity limit of our $v \sin(i)$ measurements (see Sect. 3.2).

For 12 stars we cannot derive rotation periods, because the TESS data are not (yet) available (11 stars) or the TESS light curves do not reveal any significant period (one star). All rotation periods and references are listed in Table 2. Figure 7 shows the $v \sin(i)$ values derived from the FEROS spectra vs. the stellar rotation periods. The majority of stars have rotation periods within the range of 1–10 d, with a median of 3.9 d. The shortest and longest rotation periods we find are 0.49 d (HD 191089) and 11.6 d (HD 166348).

From the rotation periods and the stellar radii (see Sect. 3.2), we compute the equatorial rotation velocities of the stars, v_{rot} , and compare them to the $v \sin(i)$ values derived from the FEROS spectra. We find that $v \sin(i) \leq v_{\text{rot}}$ for all stars (within the error bars), as one would expect when both independently determined values are correct. We then infer the inclination angles of the stellar rotation axes and their uncertainties and list the values also in Table 2.

7. Discussion

7.1. Stars with positive correlation between RV and BS

As noted in Sect. 6.2, six of our targets show a strong positive correlation ($r_P > 0.7$) between RV and BS. Figure 8 shows BS(RV) Pearson correlation coefficient, r_P , measured for the 2-week high-cadence RV data vs. effective stellar temperature, T_{eff} , for all targets in our sample. The six stars with strong positive correlation between BS and RV have certain properties in common, which distinguishes them (in a statistical sense) from most of the other targets in our survey. They all have effective temperatures > 6300 K and spectral type F5 or earlier (Figs. 4 and 8). They are younger than 300 Myr (median age 20 Myr), are fast rotators with $v \sin(i) > 40$ km/s (median 60 km/s) and rotational periods $P_{\text{rot}} < 2$ d (Figs. 7 and 10). They also have exceptionally large RV scatter (median $r_{\text{ms}}^{\text{RV}} \approx 700$ m/s) that is not reflected in the photometric variability (Fig. 6), and they have larger than average (but not unusual) fractional disc luminosities of $L_{\text{disk}}/L_* > 1e-4$ (Launhardt et al. 2020, their Fig. 6). None of these six stars shows a significant correlation between the photometric variability derived from TESS data (available for five of the six stars) and the RV variability.

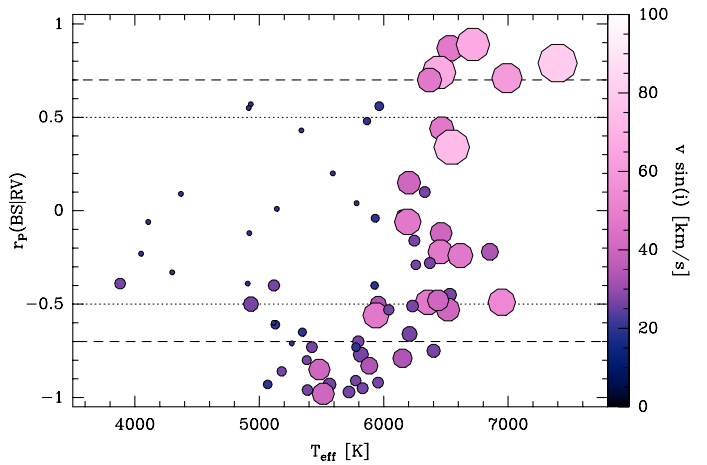


Fig. 8: BS(RV) Pearson correlation coefficient, r_P , measured for the 2-week high-cadence RV data vs. effective stellar temperature, T_{eff} , with $v \sin(i)$ encoded in marker size and color. Dotted and dashed horizontal lines mark the boundaries for what we consider here as moderate and strong correlation, respectively.

A correlation between the measured RV and BS, which is a measure of the line shape or skewness, is an indication that the RV variability is dominated by line shape variations rather than radial motion of the star. While an anti-correlation between RV and BS clearly indicates spot-related line-shape variations (Queloz et al. 2001), the underlying physical cause of a positive correlation is poorly understood. However, it has been observed and explained in a few specific cases. Martínez Fiorenzano et al. (2005) observed a similar effect in the data of HD 8071 B, where the observed star was the fainter component in a binary system. These authors explain the positive correlation between RV and BS by a possible contamination of the light entering the fiber from the brighter component that might contribute to the line profiles of the observed star. This should not be the case for the stars in our sample, because none of them has a known bright secondary component close to the fiber. Another, more likely applicable scenario was proposed for two other stars by Santos et al. (2002, HD 41004 AB) and by Günther et al. (2018, NGTS 3A). Both authors explain the correlation between RV and BS observed in their targets by line contamination due to an unresolved double-line high-contrast spectroscopic binary, i.e. the presence of a low-mass companion. In these cases, the derived RVs are a mix of true RV variability and line shape variations, which cannot be disentangled without proper modelling.

Another possible explanation could be related to pulsations, which can deform spectral lines and let them "swing" in different ways, depending on the pulsation mode (see Aerts et al. 2010, for a review). Indeed, we find sharp and significant peaks at frequencies higher than 5 d^{-1} in the TESS light curve periodograms of two of these six stars. HD 115820 (A7 V) shows a series of sharp significant periods between 20 and 35 d^{-1} (72–40 min), which are most likely Delta Scuti-like pulsations. HD 107649 (F5 V) shows a single sharp period at 7.87 d^{-1} (≈ 3 hrs), which could also hint at a certain pulsation mode. None of the other stars shows significant photometric periods in the frequency range. At this point, we only mention pulsations as a possible cause of the positive correlation between RV and BS for two of the six stars, but do not pursue further modelling if this is indeed the correct interpretation.

Because of the correlation with youth and with fractional debris disc luminosity, we also considered the possibility that the line shape variations leading to the observed positive correlation between RV and BS might be related to additional absorption lines originating from falling evaporating bodies (FEBs, or exocomets, Rebollido et al. 2020). However, since FEBs only have a tiny effect on only a few spectral lines (typically Ca II H&K), we can exclude a FEB origin of this effect.

We are currently still investigating various possibilities to explain such a positive correlation between RV and BS. At this point, we can only speculate and adopt the working hypothesis that spectral line contamination by either a still unrevealed close and low-luminosity companion is the most likely explanation for at least four of the six stars. If this is indeed true, the derived RVs are compromised and have no immediate physical meaning.

7.2. RV precision as a function of T_{eff} and $v \sin(i)$

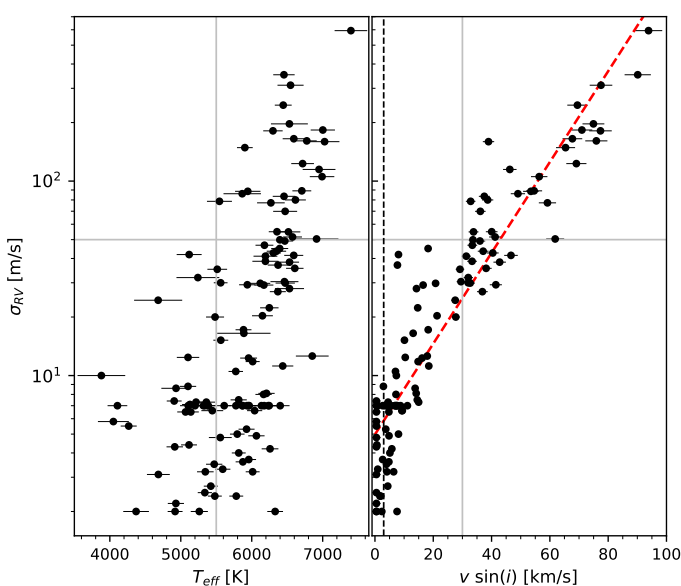


Fig. 9: Relation between single-measurement RV precision, σ_{RV} , and T_{eff} (left) and $v \sin(i)$ (right) for 121 targets from our initial input sample. All values are homogeneously derived from FEROS or HARPS spectra. Horizontal gray lines mark the threshold value of $\sigma_{RV} = 50$ m/s to select the targets for our survey. Vertical gray lines indicate the values of T_{eff} and $v \sin(i)$ below which targets are in general compatible with $\sigma_{RV} \leq 50$ m/s. The vertical dashed line on the right panel marks the lower sensitivity limit of our $v \sin(i)$ measurements. The red dashed line in the right panel shows the best fit to the correlation between $v \sin(i)$ and σ_{RV} .

Here we investigate the relation between stellar effective temperature, T_{eff} , projected radial velocity, $v \sin(i)$, and achievable RV precision, σ_{RV} . While $v \sin(i)$ directly affects the achievable RV precision, T_{eff} is indirectly related to $v \sin(i)$ and σ_{RV} via the mechanisms discussed in Sect. 2. Since the majority of our pre-selected targets does not have any useable archival FEROS or HARPS spectra from which we could directly estimate σ_{RV} , we establish these relations first for stars with available archival spectra to help guiding the target selection, and refine it then with our own FEROS spectra.

Figure 9 shows the derived relation between σ_{RV} and T_{eff} , and $v \sin(i)$ for stars with either archival¹² or our own FEROS spectra. All spectra are homogeneously reduced with the CERES pipeline (Brahm et al. 2017a) and stellar parameters derived with the ZASPE (Brahm et al. 2017b) and ATHOS (Hanke et al. 2018) pipelines. There is a clear trend indicating that σ_{RV} increases with increasing T_{eff} , although the scatter is large. All stars with $T_{\text{eff}} \leq 5500$ K have $\sigma_{RV} < 50$ m/s, which is the precision we aim for in our survey (Sect. 4.1). Stars with $T_{\text{eff}} \geq 6700$ K basically all have $\sigma_{RV} > 50$ m/s. We used this coarse figure to pre-select and prioritise those targets for which no values of $v \sin(i)$ (see below) were initially available from archival spectra or the literature, based on their T_{eff} obtained from Gaia DR2 (Gaia Collaboration et al. 2018) or from spectral energy distribution fits (Sect. 3.2). While stars with $T_{\text{eff}} \leq 5500$ K are in general safe targets and stars with $T_{\text{eff}} \geq 6700$ K are in general incompatible with our survey goals, stars with T_{eff} values in between are scheduled for obtaining test spectra to characterise their $v \sin(i)$ and σ_{RV} before a decision is made about their inclusion in the survey.

The correlation between $v \sin(i)$ and σ_{RV} is significantly tighter and we derive a relation of $\log(\sigma_{RV}[\text{m/s}]) = a(v \sin(i)[\text{km/s}]) + b$ with $a = 0.023$ and $b = 0.697$. The right panel of Fig. 9 shows that stars with $v \sin(i) \leq 30$ km/s all have $\sigma_{RV} < 50$ m/s and are thus safe survey targets, while stars with $v \sin(i) > 50$ km/s all have $\sigma_{RV} > 50$ m/s are thus in general incompatible with our survey goals. Stars with intermediate values of $v \sin(i)$ require a case-by-case inspection of test spectra before a decision is made about their inclusion in the survey.

7.3. Dependence of $v \sin(i)$ on age and T_{eff}

We use the derived values of $v \sin(i)$ to analyse their mutual dependence on T_{eff} and on the stellar age. Figure 10 shows the relation between $v \sin(i)$ and age for 68 targets already observed in high cadence, with T_{eff} coded in color (ages for two targets are not available in the literature). There is a clear correlation between T_{eff} , $v \sin(i)$, and age. The hottest and youngest stars have the largest $v \sin(i)$, and the oldest and coolest stars have the smallest $v \sin(i)$. In addition, there seems to be a general $v \sin(i)$ offset between cool and hot stars. In accordance with the reasoning outlined in Sect. 2, we assume that this $v \sin(i)$ offset is related to the presence or absence of magnetic braking. We therefore divide the stars into two groups with $T_{\text{eff}} < 6000$ K and $T_{\text{eff}} > 6000$ K, for which we perform separate fits to the relation $\log(v \sin(i)[\text{km/s}]) = a \log(\text{age}[{\text{Myr}}]) + b$. For the cooler stars with $T_{\text{eff}} < 6000$ K, we derive $a = -0.5$ and $b = 1.75$, i.e., they spin down with age much faster than stars with $T_{\text{eff}} > 6000$ K, for which we derive $a = -0.27$ and $b = 1.97$.

Comparison between Figs. 9 and 10 shows that all targets with $T_{\text{eff}} < 6000$ K down to ages of 10 Myr are suited for RV measurements with the anticipated precision of 50 m/s. Hotter stars with $T_{\text{eff}} > 6000$ K may show too large $v \sin(i)$ for precise RV measurements when they are younger than 50–100 Myr, but each star must be checked separately since the scatter in the $v \sin(i)$ vs. age relation is large.

7.4. Relation between short-term RV scatter and age

The median short-term RV scatter, $rms_{RV}(\tau=14 \text{ d})$, of our survey targets is 20 m/s (mean 130 m/s, not counting the binaries).

¹² <http://archive.eso.org>

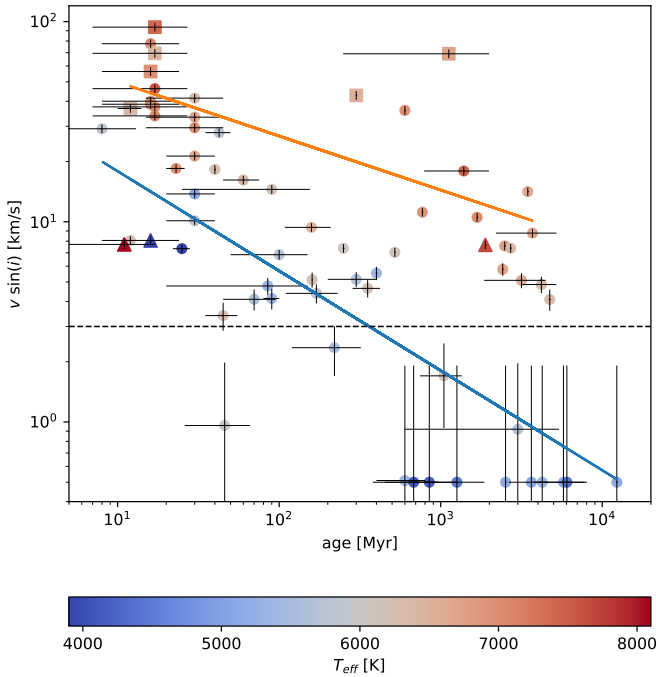


Fig. 10: Relation between $v \sin(i)$, age, and T_{eff} for stars observed in the RVSPY high-cadence program. T_{eff} is coded in color. Filled circles mark single stars, triangles show known binaries and squares show the targets with a strong positive correlation ($r_P > 0.7$) between RV and BS. Solid lines show separate linear fits to the relation between $\log(v \sin(i))$ and $\log(\text{age})$ for stars with $T_{\text{eff}} < 6000$ K (blue) and stars with $T_{\text{eff}} > 6000$ K (orange). The horizontal dashed line on the right panel marks the lower sensitivity limit of our $v \sin(i)$ measurements.

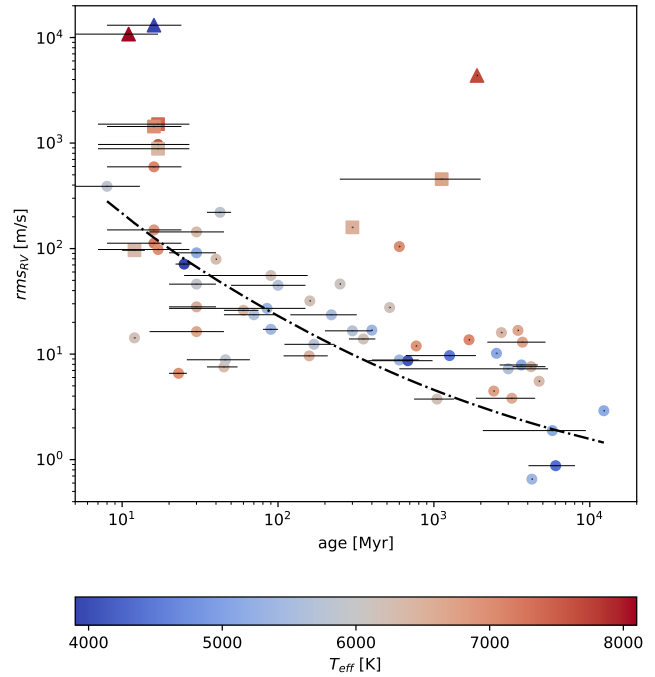


Fig. 11: Relation between RV scatter, $rms_{\text{RV}}(\tau=14 \text{ d})$, age, and T_{eff} for stars observed in the RVSPY high-cadence program. T_{eff} is coded in color. The three spectroscopic binary stars (Sect. 6.2) are marked as triangles. Squares show the targets with a strong positive correlation between RV and BS ($r_P > 0.7$). The dash-dotted line shows the relation for $\tau=10$ d derived by Brems et al. (2019). Note that for some of the stars, we do not know the age uncertainties.

Figure 11 shows the relation between $rms_{\text{RV}}(\tau=14 \text{ d})$, derived in Sect. 6.2 (see also Fig. 8), and stellar age. As expected for young stars with activity-related rotational modulation of line shapes and activity decaying with age, we find a relatively tight correlation, which agrees very well with the relation derived for a smaller sample of stars by Brems et al. (2019). The three spectroscopic binaries (Sect. 6.2) are obvious outliers since their RV variability is dominated by the orbiting companion. Most of the other outliers with excessive RV scatter show a strong positive correlation between RV and BS, which we discuss in Sect. 7.1 and about which we conclude that the measured RV variations might actually not reflect radial motions of the star. For some of the stars, we do not know the age uncertainties, such that the only other obvious outlier with excessive RV scatter, visible in Fig. 11, might actually be explained by a largely overestimated age.

7.5. Identifying targets for longer-period planet search

The observations from the first year have already shown that even with our careful target selection and the strategy for high-cadence observing campaigns, signatures of stellar activity and possible short-period companions are not easy to disentangle and will require more data. However, the high-cadence data enable us to select those stars for dedicated follow-up observations that (a) show hints of RV periodicity that cannot easily be explained by activity, (b) show a linear trend which could hint at a longer-period ($\gtrsim 10$ days) companion, or (c) have low-enough activity-related RV scatter to permit searching for even longer-

period ($\gtrsim 30$ days) companions. At least 20% of the observed stars fall in categories (a) or (b) and require follow-up observations, which we have already started during the second observing semester. We aim to complete the initial high-cadence RV survey, including the immediate follow-up observations mentioned above, within about two years (but various constraints, like weather conditions, may force us to spend three years).

Figure 12 illustrates the feasibility of and target selection for such long-term follow-up observations with adapted cadence. For all targets observed during the high-cadence campaigns, we compute the minimum mass of a hypothetical companion that might still be detected, assuming that the effective measurement precision is limited by the total RV scatter in the high-cadence data. These masses are computed assuming a 1-year orbital period (as a proxy) and assuming that the required RV semi-amplitude is at least three times larger than the "activity noise". Figure 12 shows that around five stars we could only detect stellar-mass companions with periods of one year or longer, while for another ten of the 70 targets, we could only detect brown dwarf or higher-mass companions with periods of one year or longer. All six targets with strong positive correlation between RV and BS (Sects. 6.2 and 7.1) belong to this group, i.e., we would not be able to detect longer-period planetary-mass companions around them unless we understand and can model their RV variations. Around all other targets, we could potentially detect at least substellar-mass companions in one year orbits. Among these stars we select and prioritize, after individual inspections, the targets for the second phase of our program, the monitoring for longer-period companions.

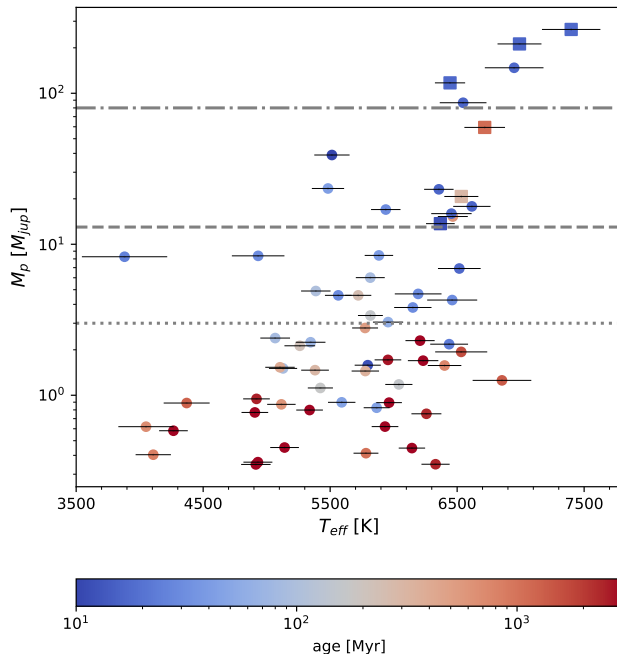


Fig. 12: Masses of $P = 1$ yr hypothetical companions that induce an RV amplitude three times larger than the activity jitter rms derived from the high-cadence observations in P101–102, plotted vs. host star T_{eff} . Ages are coded in color. Squares show the targets with a strong positive correlation ($r_P > 0.7$) between BS and RV. The dot-dashed line marks the approximate boundary between the low-mass stellar and substellar regimes and the dashed line marks the approximate boundary between the planetary and brown dwarf regimes. The dotted line marks $3 M_{\text{Jup}}$.

7.6. Comparison to other RV surveys

Dedicated RV surveys for planets around stars younger than a few hundred Myr are rare, although various larger surveys do not exclude young stars per se. However, one of the most recently published surveys by Grandjean et al. (2020) targeted 89 young (<600 Myr) A–M stars with the High Accuracy Radial velocity Planet Searcher (HARPS; Mayor et al. 2003). Most of their targets are part of the SPHERE GTO "The SpHere INfrared survey for Exoplanets" (SHINE) survey sample (Chauvin et al. 2017). Grandjean et al. (2020) did not explicitly target stars with debris discs and their sample extends to earlier spectral types (A stars) than RVSPY. Fifteen of their 89 targets are in common with our RVSPY target list, 13 of which are presented in this paper. Grandjean et al. (2020) observed each star \sim 50 times, spaced by \sim 17 nights on average, but they also tried to record data on several consecutive nights. This allowed them to get a mean time baseline of more than six years for most of the stars in their survey, while also being able to characterise the short-term activity jitter. They achieve a median short-term RV scatter of 50 m/s (mean 300 m/s), which is about 2.5 times larger than what we achieve (Sect. 7.4). It is also not obvious what the lengths and cadence of their short cadence observing series is, i.e., if stellar rotation periods and possible HCs are covered. No planetary companion was detected in this survey, but Grandjean et al. (2020) confirm the binary nature of three stars and report the detection of one close low-mass stellar companion to HIP 36985. None of these four stars is part of our survey. From the results of their survey, they derive upper limits on the occurrence rates of GPs and BDs with periods between 1 and 1000 days around young A-

to M-type stars of $2^{+3\%}_{-2\%}$ and $1^{+3\%}_{-1\%}$, respectively. Corresponding constraints based on our RVSPY survey can only be derived in 2–3 years from now, owing to the time scales of the observations.

8. Summary and conclusions

This paper presents the survey strategy, target list, and results from the first year of observations of our RV survey for giant planets and brown dwarfs around young stars with debris discs (RVSPY). Our survey list contains 113 stars of spectral types between early F and late K, with a median age of 160 Myr, and at a median distance of 44 pc. About half of the targets are also part of the NACO direct imaging survey for planets around young stars (NACO-ISPY; Launhardt et al. 2020).

Phase 1 of the RVSPY survey is dedicated to characterizing the target stars and their activity, to search for HCs, and to select the targets for which searching for longer-period companions is feasible. During the first year of the survey, 70 stars were observed, with 15 measurements per star on average, taken during about two-week long short-cadence campaigns. All observations are carried out with the FEROS spectrograph ($R = 48000$) at the La Silla observatory, in "object calibration" mode, and with integration times between 6 and 20 mins. The main results for 70 stars observed during the first year of phase 1 survey observations are summarized as follows:

- We achieve S/N ratios >100 and a median single-measurement RV precision of 11 m/s (mean 44 m/s). The achievable RV precision strongly degrades with increasing T_{eff} and $v \sin(i)$.
- We derive from the FEROS spectra values of T_{eff} between 3900 and 7300 K (median 5900 K) and of $v \sin(i)$ between <3 and 90 km/s (median 7.7 km/s).
- There is a clear trend with $v \sin(i)$ decreasing with increasing age, and a bifurcation between stars with $T_{\text{eff}} > 6000$ K having significantly larger and slower decreasing $v \sin(i)$ than cooler stars, owing to the ability for magnetic breaking.
- For 58 stars we derive stellar rotation periods (37 secure, and 21 tentative), mostly from TESS photometry. The majority of our targets have rotation periods between 1 and 10 d (median 3.9 d). We also infer inclination angles of the stellar rotation axes via stellar radii derived by fitting stellar models to observed photometry and spectra.
- The median short-term intrinsic RV scatter, $rms_{\text{RV}}(\tau=14 \text{ d})$, of our survey targets is 16 m/s (mean 126 m/s), with values ranging from about 2 m/s to 1.5 km/s. The RV scatter for the majority of our targets is caused by stellar activity and decays with age from >100 m/s at <20 Myr to <20 m/s at >500 Myr.
- We find 29 stars that show clear evidence of activity-dominated variability, but no hint for the presence of a detectable hot companion. For ten stars, we find hints for a periodic RV signal or a longer-term trend that is not correlated or anti-correlated with the BS and does not coincide with a photometric period from TESS or the literature. Follow-up observations of these targets are already on-going. Six stars show large RV variability with some (non-significant) indication of underlying periodicity and a strong positive correlation between BS and RV. We speculate that the underlying cause could be unresolved high-contrast spectroscopic companions, but cannot exclude pulsations and refer to the need of detailed modelling. For 21 stars, we can already exclude the presence of a massive (detectable) short-period companion.

- We confirm two spectroscopic binary stars (which were overlooked in the target selection), and report one previously unreported new spectroscopic binary (HD 143811) with an orbital period of ≈ 11 d.
- From the intrinsic activity-related short-term RV scatter of the target stars, we calculate the expected mass-detection thresholds for longer-period companions, and select the targets for the on-going 2nd phase of the survey, the longer-term RV monitoring with individually adapted cadence.

The initial short-cadence survey (phase 1) will be completed after about 2.5 observing years, i.e., mid to end 2020 (depending on weather conditions and telescope constraints). The 2nd, long-term monitoring phase of the survey will go on for at least 2–3 more years. A statistical analysis of the entire short-cadence survey, with detection thresholds and conclusions on the occurrence rate of HCs, will be presented in a forthcoming paper.

Acknowledgements. The authors thank Didier Queloz, Andreas Quirrenbach, Nestor Espinoza, Raffael Brahm, Damien Ségransan, Carlos Eiroa, Amelia Bayo, Daniela Paz Iglesias Vallejo and Andres Jordan for helpful discussions and feedback. A.M. acknowledges support of the DFG priority program SPP 1992 “Exploring the Diversity of Extrasolar Planets” (MU 4172/1-1). T.H. acknowledges support from the European Research Council under the Horizon 2020 Framework Program via the ERC Advanced Grant Origins 832428. G.M.K. is supported by the Royal Society as a Royal Society University Research Fellow. This work has made use of data from the European Space Agency (ESA) mission *Gaia* (<https://www.cosmos.esa.int/gaia>), processed by the *Gaia* Data Processing and Analysis Consortium (DPAC, <https://www.cosmos.esa.int/web/gaia/dpac/consortium>). Funding for the DPAC has been provided by national institutions, in particular the institutions participating in the *Gaia* Multilateral Agreement. This research has also made use of the SIMBAD database and the VizieR catalogue access tool, both operated at CDS, Strasbourg, France. The original description of the VizieR service was published in Ochsenbein et al. (2000). This paper includes data collected with the TESS mission, obtained from the MAST data archive at the Space Telescope Science Institute (STScI). Funding for the TESS mission is provided by the NASA Explorer Program. STScI is operated by the Association of Universities for Research in Astronomy, Inc., under NASA contract NAS 5–26555.

References

- Aerts, C., Christensen-Dalsgaard, J., & Kurtz, D. W. 2010, Asteroseismology
- Anderson, E. & Francis, C. 2012, *Astronomy Letters*, 38, 331
- Apai, D., Janson, M., Moro-Martín, A., et al. 2008, *ApJ*, 672, 1196
- Bailer-Jones, C. A. L., Rybizki, J., Fouesneau, M., Mantelet, G., & Andrae, R. 2018, *AJ*, 156, 58
- Bedding, T. R., Murphy, S. J., Hey, D. R., et al. 2020, arXiv e-prints, arXiv:2005.06157
- Biazzo, K., Frasca, A., Catalano, S., & Marilli, E. 2007, *Astronomische Nachrichten*, 328, 938
- Boisse, I., Moutou, C., Vidal-Madjar, A., et al. 2009, *A&A*, 495, 959
- Bouvier, J., Matt, S. P., Mohanty, S., et al. 2014, in *Protostars and Planets VI*, ed. H. Beuther, R. S. Klessen, C. P. Dullemond, & T. Henning, 433
- Brahm, R., Jordán, A., & Espinoza, N. 2017a, *PASP*, 129, 034002
- Brahm, R., Jordán, A., Hartman, J., & Bakos, G. 2017b, *MNRAS*, 467, 971
- Brems, S. S., Kürster, M., Trifonov, T., Reffert, S., & Quirrenbach, A. 2019, *A&A*, 632, A37
- Butler, R. P., Vogt, S. S., Laughlin, G., et al. 2017, *AJ*, 153, 208
- Carpenter, J. M., Bouwman, J., Mamajek, E. E., et al. 2009, *ApJS*, 181, 197
- Casagrande, L., Schönrich, R., Asplund, M., et al. 2011, *A&A*, 530, A138
- Chauvin, G., Desidera, S., Lagrange, A. M., et al. 2017, in SF2A-2017: Proceedings of the Annual meeting of the French Society of Astronomy and Astrophysics, ed. C. Reylé, P. Di Matteo, F. Herpin, E. Lagadec, A. Lançon, Z. Meliani, & F. Royer, Di
- Chen, C. H., Mittal, T., Kuchner, M., et al. 2014, *ApJS*, 211, 25
- Cotten, T. H. & Song, I. 2016, *ApJS*, 225, 15
- Cox, A. N. 2000, Allen’s astrophysical quantities
- Dawson, R. I. & Johnson, J. A. 2018, *ARA&A*, 56, 175
- Desidera, S., Covino, E., Messina, S., et al. 2015, *A&A*, 573, A126
- Desort, M., Lagrange, A. M., Galland, F., Udry, S., & Mayor, M. 2007, *A&A*, 473, 983
- Duncan, D. K., Vaughan, A. H., Wilson, O. C., et al. 1991, *ApJS*, 76, 383
- Eiroa, C., Marshall, J. P., Mora, A., et al. 2013, *A&A*, 555, A11
- Gaia Collaboration, Brown, A. G. A., Vallenari, A., et al. 2018, *A&A*, 616, A1
- Gaia Collaboration, Prusti, T., de Bruijne, J. H. J., et al. 2016, *A&A*, 595, A1
- Gorynya, N. A. & Tokovinin, A. 2018, *MNRAS*, 475, 1375
- Grandjean, A., Lagrange, A. M., Keppler, M., et al. 2020, *A&A*, 633, A44
- Gregory, S. G. 2017, in *IAU Symposium*, Vol. 328, *Living Around Active Stars*, ed. D. Nandy, A. Valio, & P. Petit, 252–263
- Günther, M. N., Queloz, D., Gillen, E., et al. 2018, *MNRAS*, 478, 4720
- Hanke, M., Hansen, C. J., Koch, A., & Grebel, E. K. 2018, *A&A*, 619, A134
- Hatzes, A. P. 2002, *Astronomische Nachrichten*, 323, 392
- Hauser, M. G., Kelsall, T., Moseley, S. H., et al. 1989, in *BAAS*, Vol. 21, *Bulletin of the American Astronomical Society*, 1219
- Herbst, W., Bailer-Jones, C. A. L., Mundt, R., Meisenheimer, K., & Wackermann, R. 2002, *A&A*, 396, 513
- Høg, E., Fabricius, C., Makarov, V. V., et al. 2000, *A&A*, 355, L27
- Husser, T.-O., Wende-von Berg, S., Dreizler, S., et al. 2013, *A&A*, 553, A6
- Ibukiyama, A. & Arimoto, N. 2002, *A&A*, 394, 927
- Johns, C. M. & Basri, G. 1995, *AJ*, 109, 2800
- Kaufer, A., Stahl, O., Tubbesing, S., et al. 1999, *The Messenger*, 95, 8
- Kennedy, G. M. & Wyatt, M. C. 2014, *MNRAS*, 444, 3164
- Keppler, M., Benisty, M., Müller, A., et al. 2018, *A&A*, 617, A44
- Kürster, M., Endl, M., Rouesnel, F., et al. 2003, *A&A*, 403, 1077
- Lachaume, R., Dominik, C., Lanz, T., & Habing, H. J. 1999, *A&A*, 348, 897
- Launhardt, R., Henning, T., Quirrenbach, A., et al. 2020, arXiv e-prints, arXiv:2002.01807
- Lin, D. N. C. & Papaloizou, J. 1986, *ApJ*, 309, 846
- Lo Curto, G., Pepe, F., Avila, G., et al. 2015, *The Messenger*, 162, 9
- Mamajek, E. E. & Bell, C. P. M. 2014, *MNRAS*, 445, 2169
- Mamajek, E. E. & Hillenbrand, L. A. 2008, *ApJ*, 687, 1264
- Martínez Fiorenzano, A. F., Gratton, R. G., Desidera, S., Cosentino, R., & Endl, M. 2005, *A&A*, 442, 775
- Mayor, M., Pepe, F., Queloz, D., et al. 2003, *The Messenger*, 114, 20
- Meshkat, T., Mawet, D., Bryan, M. L., et al. 2017, *AJ*, 154, 245
- Messina, S., Lanzafame, A. C., Feiden, G. A., et al. 2016, *A&A*, 596, A29
- Messina, S., Millward, M., Buccino, A., et al. 2017, *A&A*, 600, A83
- Meyer, M. R., Hillenbrand, L. A., Backman, D., et al. 2006, *PASP*, 118, 1690
- Montes, D., López-Santiago, J., Gálvez, M. C., et al. 2001, *MNRAS*, 328, 45
- Moór, A., Kóspál, Á., Ábrahám, P., et al. 2015, *MNRAS*, 447, 577
- Moór, A., Kóspál, Á., Ábrahám, P., et al. 2016, *ApJ*, 826, 123
- Müller, A., Keppler, M., Henning, T., et al. 2018, *A&A*, 617, L2
- Ochsenbein, F., Bauer, P., & Marcout, J. 2000, *A&AS*, 143, 23
- Plavchan, P., Werner, M. W., Chen, C. H., et al. 2009, *ApJ*, 698, 1068
- Povich, M. S., Giampapa, M. S., Valenti, J. A., et al. 2001, *AJ*, 121, 1136
- Queloz, D., Henry, G. W., Sivan, J. P., et al. 2001, *A&A*, 379, 279
- Rameau, J., Chauvin, G., Lagrange, A. M., et al. 2013, *ApJ*, 779, L26
- Ramírez, I., Fish, J. R., Lambert, D. L., & Allende Prieto, C. 2012, *ApJ*, 756, 46
- Rebollido, I., Eiroa, C., Montesinos, B., et al. 2020, arXiv e-prints, arXiv:2003.11084
- Reiners, A., Joshi, N., & Goldman, B. 2012, *AJ*, 143, 93
- Rhee, J. H., Song, I., Zuckerman, B., & McElwain, M. 2007, *ApJ*, 660, 1556
- Ricker, G. R., Winn, J. N., Vanderspek, R., et al. 2015a, *Journal of Astronomical Telescopes, Instruments, and Systems*, 1, 014003
- Ricker, G. R., Winn, J. N., Vanderspek, R., et al. 2015b, *Journal of Astronomical Telescopes, Instruments, and Systems*, 1, 014003
- Santos, N. C., Mayor, M., Naef, D., et al. 2002, *A&A*, 392, 215
- Schneider, J., Dedieu, C., Le Sidaner, P., Savalle, R., & Zolotukhin, I. 2011, *A&A*, 532, A79
- Tal-Or, L., Trifonov, T., Zucker, S., Mazeh, T., & Zechmeister, M. 2019, *MNRAS*, 484, L8
- Trifonov, T. 2019, The Exo-Striker: Transit and radial velocity interactive fitting tool for orbital analysis and N-body simulations
- Trifonov, T., Tal-Or, L., Zechmeister, M., et al. 2020, *A&A*, 636, A74
- van Leeuwen, F. 2010, *Space Sci. Rev.*, 151, 209
- Vican, L. 2012, *AJ*, 143, 135
- Vogt, S. S., Allen, S. L., Bigelow, B. C., et al. 1994, *Society of Photo-Optical Instrumentation Engineers (SPIE) Conference Series*, Vol. 2198, HIRES: the high-resolution echelle spectrometer on the Keck 10-m Telescope, ed. D. L. Crawford & E. R. Craine, 362
- Wahhaj, Z., Milli, J., Kennedy, G., et al. 2016, *A&A*, 596, L4
- Weise, P., Launhardt, R., Setiawan, J., & Henning, T. 2010, *A&A*, 517, A88
- Williams, J. P. & Cieza, L. A. 2011, *ARA&A*, 49, 67
- Wright, J. T., Marcy, G. W., Howard, A. W., et al. 2012, *ApJ*, 753, 160
- Wright, N. J., Drake, J. J., Mamajek, E. E., & Henry, G. W. 2011, *ApJ*, 743, 48
- Yelverton, B., Kennedy, G. M., & Su, K. Y. L. 2020, *MNRAS*, 495, 1943
- Yelverton, B., Kennedy, G. M., Su, K. Y. L., & Wyatt, M. C. 2019, *MNRAS*, 488, 3588
- Zechmeister, M. & Kürster, M. 2009, *A&A*, 496, 577
- Zuckerman, B., Rhee, J. H., Song, I., & Bessell, M. S. 2011, *ApJ*, 732, 61
- Zuckerman, B. & Song, I. 2004, *ARA&A*, 42, 685

Appendix A: Activity analysis of HD 38949

Here we demonstrate our stellar activity analysis and characterization (as described in Sect. 5.2) exemplary for the star HD 38949. Figures A.1a and A.1b show the available RV data and the corresponding GLS periodogram and window function, respectively. There are peak-to-peak variations of ≈ 60 m/s observed in the RV data with periods at 3.7 d and 8.3 d. A combined sinusoidal fit of these two periods is shown as red line in Fig. A.1a. Figure A.2 shows that there is a significant linear correlation ($r = -0.81$, $p = 8.3 \cdot 10^{-5}$) between the measured bisector velocity-span and the RV, indicating that the observed periodic RV variations are caused by surface features on the rotating star.

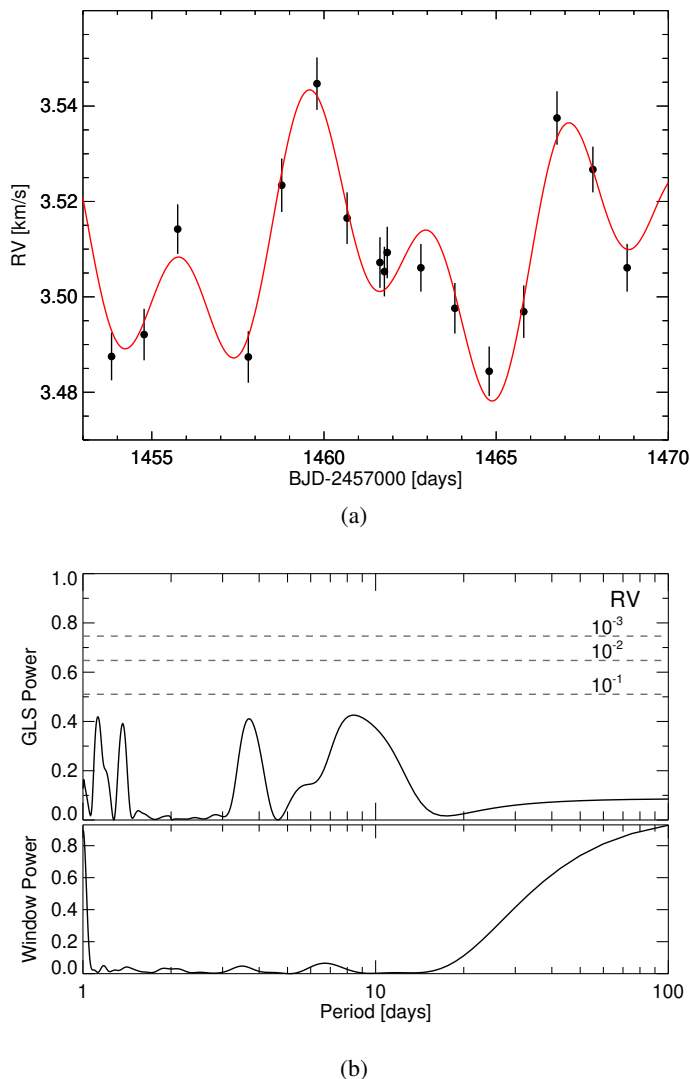


Fig. A.1: (a) RVSPY data (black symbols) of HD 38949 and a combined sinusoidal fit to the data for the 3.7 d and 8.3 d period is shown in red. (b) GLS periodogram and window function of the RV data. The horizontal lines mark different false alarm probabilities.

Since HD 38949 has publicly available data from TESS¹³, this can be verified by looking at the photometric variability. Figure A.3a shows the time series of photometric data after removing a long-term linear trend. The corresponding GLS pe-

¹³ Obtained from <https://dx.doi.org/10.17909/t9-h5bx-p296>.

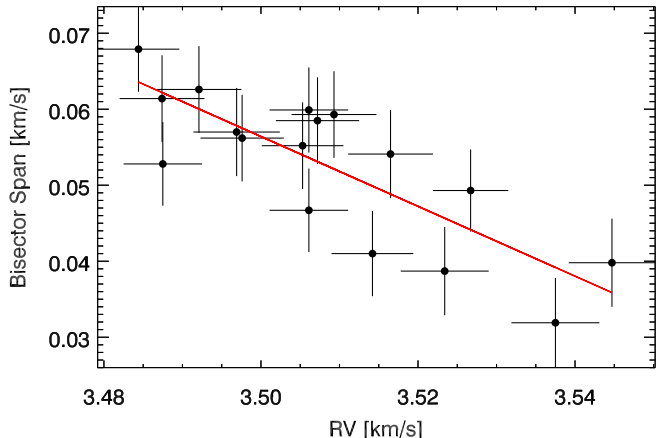


Fig. A.2: Linear anti-correlation between RV and bisector velocity-span. The red line is a linear fit.

riodogram (Fig. A.3b) shows two significant peaks at 3.8 d and 6.9 d, which are similar to the periods found in the RV data. A possible explanation for this behavior could be two dark spots or spot groups placed on approximate opposite sides of the stellar surface. The rotation period of HD 38949 was already estimated earlier from photometric measurements by Wright et al. (2011) to be ≈ 7.6 d, which agrees well with the longer of the two periods we find in both the RV and the TESS photometry data.

To further verify the hypothesis that we observe a RV variation which is caused rotational modulation of stellar spots, we compute two-dimensional versions of GLS periodograms for the spectral lines Ca II H&K and H α by shifting all spectra to their rest wavelength and computing a periodogram for each velocity channel (Figs. A.4a through A.4c). These 2D periodograms show that all three line cores exhibit periodic variability on a time scale of $\approx 6\text{--}7$ days. This subtle variability is not readily detected in the corresponding line EWs, which are integral quantities describing only the total intensity of the entire line. In addition, we also compute the Ca II H&K S -index and the H α index (Sect. 5.2) and show the corresponding GLS periodograms in Figs. A.4d and A.4e. Like the line cores in the 2D periodograms, both quantities display significant variability on a time scale of $>6\text{--}7$ days, which agrees well with the longer of the two periods we find in both the RV and the TESS photometry data. We therefore conclude for HD 38949 that the observed RV variations are caused by rotational modulation of stellar spots. This analysis also demonstrates the importance of using several indicators and methods simultaneously to identify and quantify processes related to stellar activity.

We perform a similar activity analysis for all stars in our sample in a semi-automatic fashion. However, only half of the twelve stars that show a clear anti-correlation between RV and BS (Sect. 6.2) also show a significant periodicity in the TESS photometric data.

Appendix B: Activity analysis of CPD–72 2713

A good example of a star with an interesting RV periodicity, that is not obviously doomed to be activity-related by a clear anti-correlation between RV and BS, is CPD–72 2713. This star was observed in high cadence in August 2018 and was initially classified as a "HC candidate" because of a significant

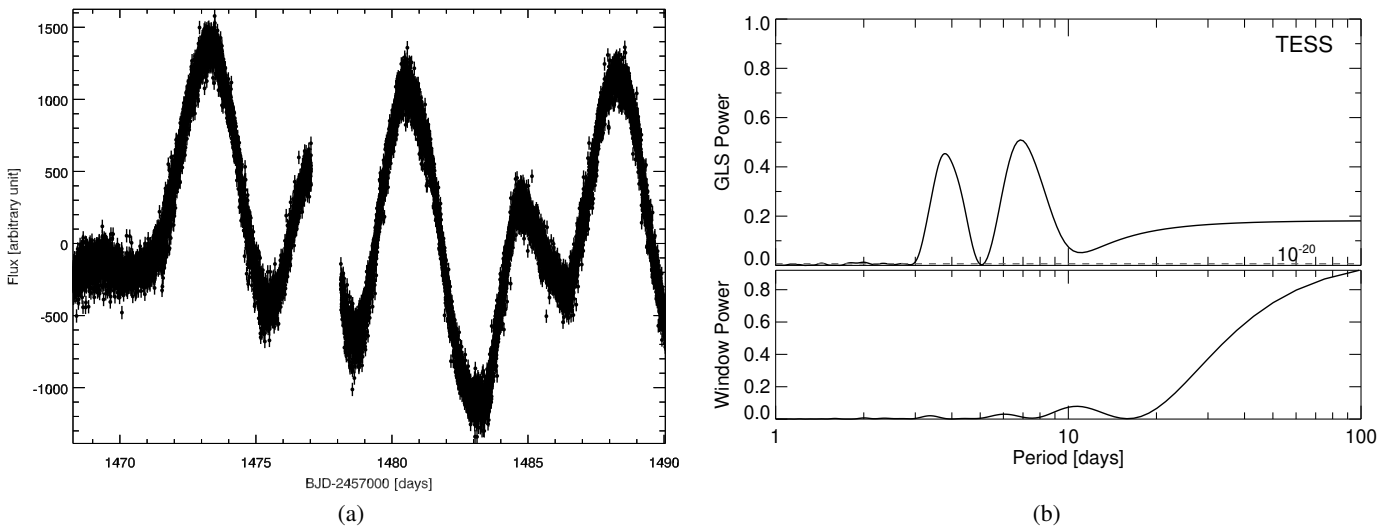


Fig. A.3: (a) TESS photometry of HD 38949, after removing a long-term linear trend. (b) GLS periodogram and window function of TESS photometry.

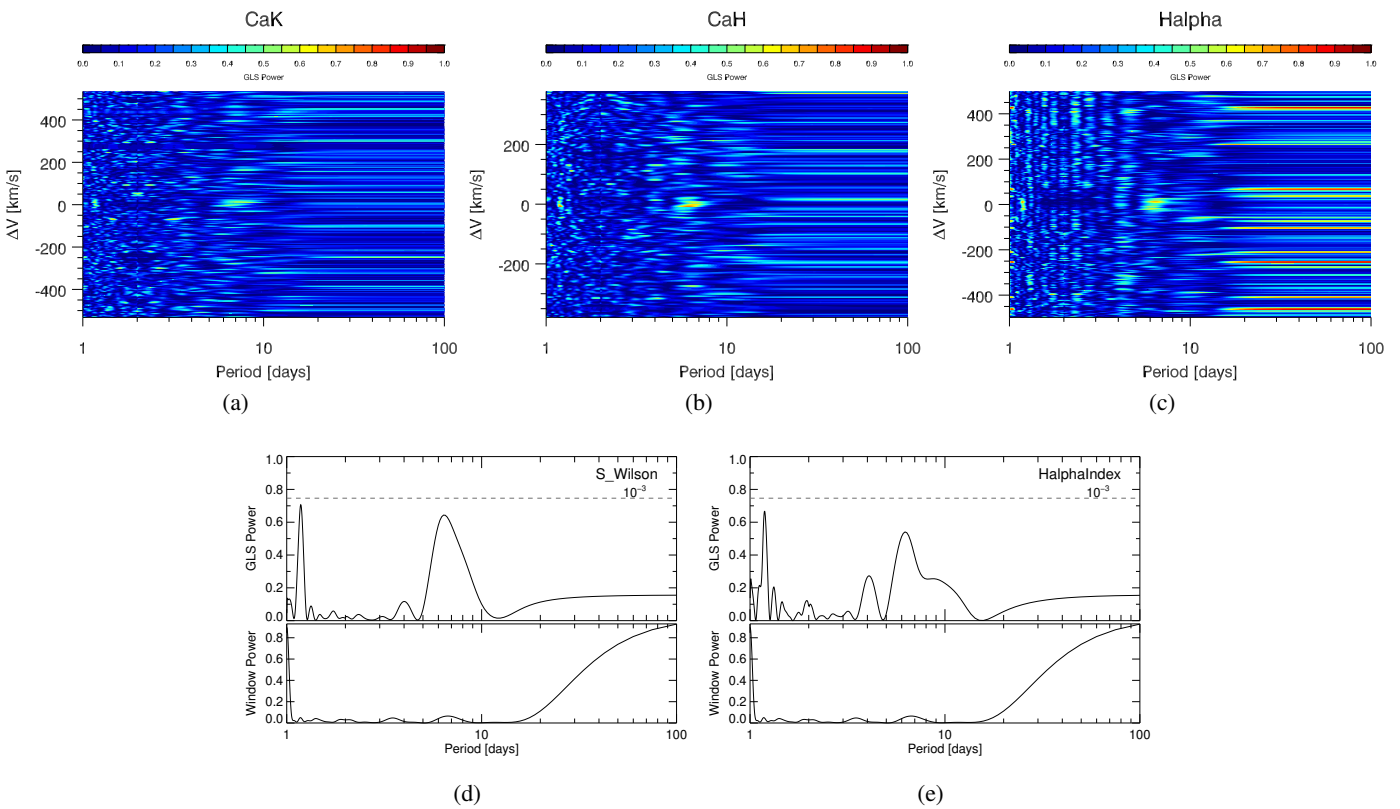


Fig. A.4: (a–c) 2D GLS periodograms of Ca II K, H, and H α . (d) GLS periodogram of the S -index based on flux measurements of Ca II H&K. (e) GLS periodogram of the H α index. All three lines display a clear variability on a time scale of 6–7 days.

RV signal at $P_{\text{RV}} = 4.57 \pm 0.10$ d and the absence of a clear anti-correlation between RV and BS. However, a photometric study by Messina et al. (2017) reports a stellar rotational period of $P_{\text{rot}} = 4.46$ d, which is very close to the RV period we find. The TESS data (released in December 2018) also confirm the presence of a significant signal at $P_{\text{phot}} = 4.42 \pm 0.002$ d, which is clearly related to the rotational modulation caused by stellar activity. Figure B.1 illustrates (from top to bottom) the RV and

BS time series (RVSPY data), the GLS periodograms of the RVs and the photometric TESS data, as well as the photometric data time series. The additional signal at a period of 1.3 d in the GLS periodogram of the RV data is an alias of the real signal at 4.57 d.

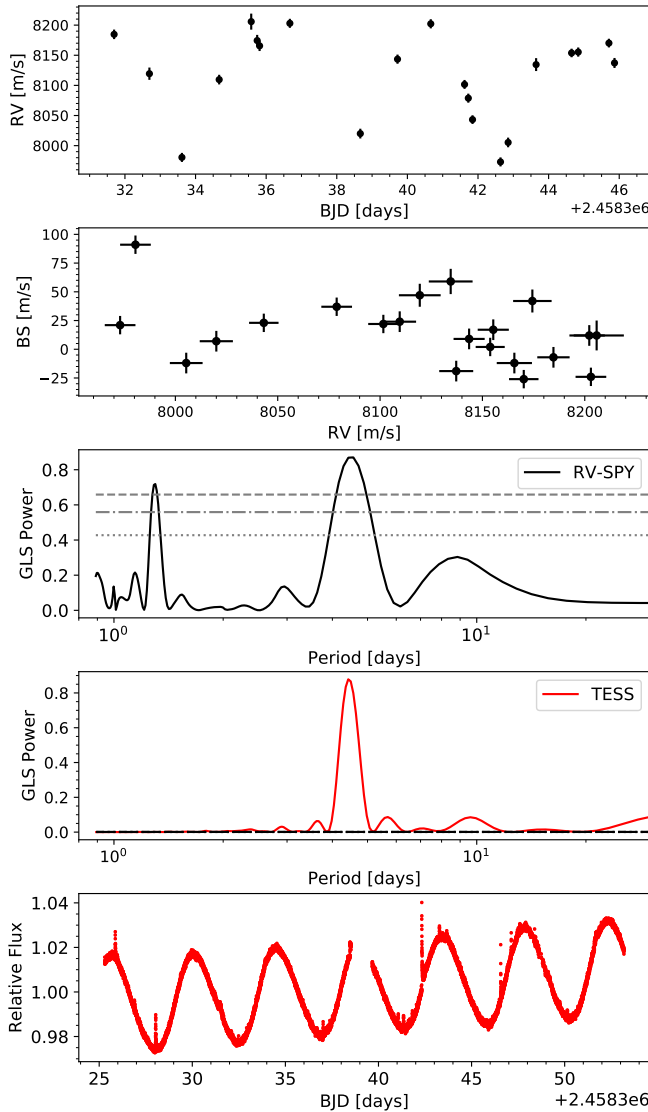


Fig. B.1: RVSPY and TESS data for CPD–72 2713. The panels show (from top to bottom): the RV time series, the relation between RV and BS, the GLS periodogram of the RVs and of the photometric data (measured by TESS), and the TESS time series. All data products of the RVSPY program are shown in black, all TESS data products are shown in red. Horizontal lines in the GLS periodogram of RVs reflect the 0.1%, 1% and 10% false alarm probabilities (from top to bottom); the dashed line in the GLS periodogram of photometric data reflects 0.1% false alarm probability.

Table 2: Physical parameters of Stars observed in high cadence during ESO periods 101 and 102

Name	RA(J2000) [hh:mm:ss]	DEC(J2000) [dd:mm:ss]	dist. ^a [pc]	V^b [mag]	SpT ^c	T_{eff}^d [K]	$\log(L_*)^e$ [L_{\odot}]	$v \sin i^f$ [km s ⁻¹]	age ^g [Myr]	Ref. ^g	P_{rot}^h [d]	Incl. ^h [deg]	Notes ⁱ
HD 377	00:08:25.7	06:37:00.5	38.5	7.59	G2 V	5816±114	0.07	14.5	90±65	2	1
HD 1466	00:18:26.0	-63:28:38.5	42.9	7.46	G0 V	6151±147	0.20	21.3	30±10	20	2.4±0.1	73±19	2
HD 1835	00:22:51.6	-12:12:34.5	21.3	6.39	G3 V	5775±102	0.04	7.0	520	18	(3.82±0.05)	(31±3)	5
HD 3296	00:36:01.9	-05:34:14.6	44.9	6.71	F6 V	6532±205	0.53	14.2	1680	5	2.3±0.1	19±2	2
HD 3670	00:38:56.7	-52:32:03.4	77.4	8.21	F5 V	6461±197	0.40	29.5	30±15	5	0.74±0.05	41±4	2
HD 5133	00:53:01.1	-30:21:24.9	14.0	7.17	K2.5 V	4907±105	-0.54	0.5	3640±1000	7	(8.1±0.1)	(19±20)	4
HD 5349	00:55:11.8	-16:58:17.6	59.2	7.91	K0 IV	4931±114	0.42	0.5	12300	5	(5.0±0.5)	(4±5)	3
HD 7570	01:15:11.1	-45:31:54.0	15.2	4.96	F9 V	6144±104	0.29	5.1	3162±1304	9	5.93±0.05	30±3	2
HIP 6276	01:20:32.2	-11:28:02.5	35.3	8.43	G9 V	5346±117	-0.28	4.1	70±25	21	5.94±0.05	35±6	2
HD 10008	01:37:35.4	-06:45:36.7	24.0	7.66	K0.5 V	5338±105	-0.33	0.9	3000±2400	4	(7.47±0.05)	(16±16)	4
HD 13246	02:07:26.0	-59:40:45.8	45.6	7.50	F8 V	6193±184	0.24	33.3	30±15	20	1.71±0.05	90±10	2
HD 14082B	02:17:24.7	28:44:30.3	39.7	7.74	G2 V	5796±103	0.03	8.1	12	22	1
HD 15060	02:23:35.5	-55:37:00.5	79.0	7.02	F5 V	6258±118	0.88	5.8	2420	5	(6.3±0.1)	(18±2)	6
HD 16673	02:40:12.4	-09:27:10.4	21.9	5.80	F8 V	6246±116	0.29	7.7	1890	18	4.25±0.05	33±3	2
HD 17925	02:52:31.9	-12:46:09.3	10.4	6.05	K1 V	5120±111	-0.40	4.1	90±10	20	6.92±0.05	57±10	2
HD 19668	03:09:42.2	-09:34:45.6	38.7	8.48	G8 V	5387±116	-0.24	6.9	100±50	6	(5.64±0.05)	(67±10)	4
HD 22484	03:36:52.4	00:24:06.0	14.0	4.30	F9 V	5964±101	0.50	4.9	4200±1000	5	1
HD 23356	03:43:55.4	-19:06:39.2	13.9	7.10	K2 V	4915±116	-0.52	0.5	5750±6400	16	(10.8±0.1)	(26±28)	4
HD 23484	03:44:09.2	-38:16:54.4	16.2	7.00	K2 V	5116±112	-0.39	0.7	600±200	11	1, 7
HD 33081	05:07:08.7	-17:17:59.7	53.8	7.04	F7 V	6330±111	0.56	7.6	2490	5	7.8±0.1	48±4	2
SAO 150676	05:40:20.7	-19:40:10.8	73.0	8.96	G2 V	5483±127	0.06	27.7	63.1±10.0	7	1.70±0.05	56±7	2
HD 38397	05:43:35.8	-39:55:24.7	53.7	8.14	G0 V	5956±119	0.13	16.2	60±15	20	2.26±0.05	40±4	2
HD 38949	05:48:20.1	-24:27:49.9	44.6	7.80	G1 V	5955±105	0.13	7.4	2710	5	(7.29±0.05)	(80±24)	4
HD 40136	05:56:24.3	-14:10:04.9	14.5	3.71	F1 V	6853±231	0.74	17.9	1390±600	5	0.96±0.05	12±1	2
HD 43989	06:19:08.1	-03:26:20.0	51.9	7.95	G0 V	5938±116	0.19	41.5	30±15	21	1.361±0.05	71±17	2
HD 48370	06:43:01.0	-02:53:19.3	36.0	7.91	G5 V	5564±105	-0.11	10.1	30±10	14	5.21±0.1	90±10	2
HD 50571	06:50:01.0	-60:14:56.9	34.0	6.10	F5 V	6533±134	1.26	42.8	300±0	5	1.89±0.1	90±10	2
HD 53143	06:59:59.9	-61:20:12.6	18.4	6.81	G9 V	5381±109	-0.23	5.2	300±100	17	(4.85±0.05)	(35±4)	5
HD 57703	07:23:04.6	18:16:24.3	43.8	6.77	F2	6466±118	0.48	36.0	600	5	1
HD 59659	07:28:30.1	-49:08:58.9	87.4	8.79	F7 V	6203±145	0.28	33.4	1.61±0.05	61±10	2
HD 59967	07:30:42.5	-37:20:21.7	21.8	6.64	G3 V	5777±108	-0.05	4.3	353±68	15	5.22±0.05	31±4	2
HD 72687	08:33:15.4	-29:57:23.9	45.4	8.26	G5 V	5721±103	-0.05	7.4	250	3	3.88±0.05	44±4	2
HD 76151	08:54:18.0	-05:26:04.1	16.8	6.00	G3 V	5782±98	-0.01	1.7	1047±301	9	5.2±1	9±11	2
HD 76748	08:54:51.2	-63:42:07.0	48.9	9.44	K0 V	5141±113	-0.29	0.5	4250	5	(2.4±0.8)	(5±7)	8
HD 76653	08:55:11.8	-54:57:56.8	24.3	5.70	F6 V	6401±132	0.40	11.1	770	5	2.11±0.05	21±2	2
CD-49 3972	08:56:10.8	-49:29:26.6	139.0	10.24	F5	5927±113	0.13	3.7	(7.5±2.5)	(27±15)	8
HD 84075	09:36:17.8	-78:20:41.6	64.0	8.59	G2 V	5884±112	0.12	18.3	40	5	2.5±0.1	56±8	2
HD 90905	10:29:42.3	01:29:29.1	31.0	6.88	G1 V	6041±107	0.16	9.4	158.5±50	3	(2.6±0.1)	(18±2)	1, 12
HD 92945	10:43:28.4	-29:03:51.0	21.5	7.72	K1 V	5067±117	-0.43	4.8	85±65	13	(7.9±0.1)	(77±29)	4
HD 93932	10:50:25.5	-15:06:15.1	50.8	7.53	G3 V	5932±105	0.40	4.1	4730	5	3
HD 101259	11:39:00.4	-24:43:15.9	67.6	6.42	G7 V	4920±105	1.32	0.5	2520	5	(0.98±0.1)	(0±1)	6, 11
HD 102458	11:47:24.6	-49:53:02.9	113.0	9.07	G5 V	5514±139	0.43	29.2	8±5	20	2.02±0.05	45±5	2

Continued on next page

Table 2: – continued from previous page

Name	RA(J2000) [hh:mm:ss]	DEC(J2000) [dd:mm:ss]	dist. ^a [pc]	V ^b [mag]	SpT ^c	T _{eff} ^d [K]	log(L _*) ^e [L _⊙]	v sin <i>i</i> ^f [km s ⁻¹]	age ^g [Myr]	Ref. ^g	P _{rot} ^h [d]	Incl. ^h [deg]	Notes ^h
HD 104231	12:00:09.4	-57:07:02.0	102.4	8.54	F5 V	6517±168	0.51	33.8	17±10	5	1
HD 107146	12:19:06.6	16:32:55.2	27.5	7.04	G2 V	5817±98	0.00	5.1	160	3	(3.7±0.2)	(35±5)	1, 7
HD 107649	12:22:24.9	-51:01:34.4	108.0	8.78	F5 V	6444±119	0.45	69.5	17±10	5	0.94±0.05	65±15	2
HD 109832	12:38:42.8	-68:45:49.1	108.0	8.09	A9 V	6949±231	0.72	46.3	17±10	5	(1.19±0.05)	(42±5)	4
HD 111520	12:50:19.7	-49:51:49.0	108.6	8.87	F5 V	6455±159	0.43	37.5	17±10	5	(1.53±0.1)	(52±9)	9
HD 111631	12:50:43.6	-00:46:01.8	10.7	8.49	M1 V	4050±218	-1.00	0.5	680±300	18	1
HD 114082	13:09:16.2	-60:18:30.1	95.4	8.21	F3 V	6616±147	0.58	38.7	16±8	19	1
HD 115820	13:20:26.8	-49:13:25.2	115.5	7.95	A7 V	7398±230	0.85	93.9	17±10	5	(0.52±0.05)	(36±11)	9, 10
MML 36	13:37:57.3	-41:34:42.0	99.5	10.08	K0 IV	4933±207	0.00	13.8	30±10	20	4.74±0.05	72±13	2
HD 118972	13:41:04.2	-34:27:51.0	15.7	6.92	K0 V	5105±116	-0.39	5.6	400	5	(4.5±0.2)	(38±6)	5
HD 122948	14:04:43.2	04:46:45.8	44.0	8.51	G5	5591±108	-0.17	1.0	46±20	5	1
HD 131156	14:51:23.3	19:06:02.3	6.73	4.54	G8 V	5423±99	-0.19	4.4	300	18	1
HD 139664	15:41:11.5	-44:39:38.0	17.4	4.64	F5 IV	6717±160	0.53	69.1	1122±873	9	0.89±0.05	63±13	2
HD 141011	15:48:24.8	-42:37:05.0	128.1	8.97	F5 V	6547±184	0.54	77.5	16±8	5	0.94±0.05	71±21	2
HD 141521	15:51:13.7	-42:18:51.3	131.3	10.25	G8 IV	5118±176	0.39	8.1	16±8	5	4.89±0.1	24±2	2
HD 143811	16:03:33.4	-30:08:13.4	136.6	8.91	F5 V	6371±145	0.63	7.7	11±6	5	4.4±0.1	22±2	2
HD 145560	16:13:34.3	-45:49:03.7	120.0	8.90	F5 V	6356±116	0.51	40.0	16±8	5	1.41±0.05	48±7	2
HD 145972	16:16:03.8	-49:04:29.4	125.4	8.40	F0 V	6991±173	0.73	56.3	16±8	5	1.5±0.1	90±10	2
HD 166348	18:12:21.3	-43:26:37.8	13.2	8.38	K7 V	4266±113	-0.88	0.5	6040±2000	18	11.58±0.05	32±36	2
HD 181327	19:22:58.9	-54:32:16.3	48.2	7.04	F6 V	6437±149	0.46	18.5	23±3	10	1.54±0.05	39±4	2
HD 191089	20:09:05.2	-26:13:26.5	50.1	7.18	F5 V	6368±113	0.44	36.8	12±2	22	(0.49±0.1)	(16±4)	1, 13
HD 191849	20:13:52.8	-45:09:49.1	6.16	7.97	M0 V	4107±139	-1.23	0.5	850±400	18	1
HD 199260	20:56:47.3	-26:17:47.0	21.3	5.70	F6 V	6208±115	0.29	14.2	3460	8	4.13±0.05	77±17	2
CPD-722713	22:42:48.9	-71:42:21.2	36.6	10.57	K7 V	3881±336	-0.73	7.3	25±3	12	4.43±0.05	42±4	2
HD 218340	23:08:12.2	-63:37:40.8	56.1	8.44	G3 V	5866±102	0.06	3.4	45±10	5	7.65±0.05	29±6	2
HD 218511	23:09:41.4	-67:43:56.3	14.8	8.29	K5 V	4370±181	-0.81	0.5	1260±600	18	8.46±0.05	21±23	2
HD 219482	23:16:57.7	-62:00:04.3	20.5	5.66	F6 V	6232±120	0.28	8.8	3700±1500	1	2.18±0.05	19±2	2
HD 223340	23:48:50.5	-28:07:15.7	44.2	9.28	K1 V	5261±121	-0.35	2.4	220±100	18	(5.87±0.1)	(12±13)	4

(a) Distances are inferred from *Gaia* DR2 parallaxes with the method described by Bailer-Jones et al. (2018). (b) Visual magnitudes are taken from The Hipparcos and Tycho Catalogues and from SIMBAD. (c) Spectral types are taken from FEROS spectra with the ATHOS pipeline (Hanke et al. 2018).

(e) Bolometric stellar luminosities, L_* , are derived by fitting stellar atmosphere models (PHOENIX; Husser et al. 2013) to observed photometry compiled from various data bases (see Sect. 3.2). (f) Values of $v \sin(i)$ are derived from FEROS spectra using the ZASPE pipeline (Brahm et al. 2017b). (g) Ages and their uncertainties, where available, are compiled from the literature with references given in the next column. (h) Stellar rotational periods and inclinations derived from TESS data, $v \sin(i)$, and R_* as described in Sect. 6.3. Rotation periods, and consequently inclination, we consider as insecure, are set in brackets. Notes: (1) no TESS data available, (2) Single dominant and significant period, (3) No significant period in TESS data, (4) The longer of two significant periods with ratio $\approx 2:1$ is chosen as P_{rot} , (5) Only the shorter of two significant periods with ratio $\approx 2:1$ is compatible with $v \sin(i)$, (6) Single dominant, but not significant period, (7) No TESS data available, but marginally significant RV period and strong anti-correlation between RV and B_S , P_{rot} highly uncertain, (8) No significant period, but periodogram power over range of periods, adopted mean and range as P_{rot} and uncertainty, (9) The most significant TESS period cannot be P_{rot} given R_* and $v \sin(i)$. Instead, a shorter and less significant period was identified to more likely represent P_{rot} (see text), (10) Series of sharp significant periods between 20 and 35 d⁻¹ (72–40 min), most likely Delta Scuti pulsations, (11) Series of periods between 8 and 12 d⁻¹ (3–2 hrs), pulsations? (12) Tentative period derived from the Spitzer Legacy Science Program Formation and Evolution of Planetary Systems data (FEPS; Meyer et al. 2006) by Wright et al. (2011), (13) Tentative period derived from Hipparchos data by Desidera et al. (2015)

- References.** (1) Anderson & Francis (2012); (2) Apai et al. (2008); (3) Carpenter et al. (2009); (4) Casagrande et al. (2011); (5) Chen et al. (2014); (6) Desidera et al. (2015); (7) Eiroa et al. (2013); (8) Ibukiyana & Arimoto (2002); (9) Lachaume et al. (1999); (10) Mamajek & Bell (2008); (11) Mamajek & Hillenbrand (2001); (14) Moón et al. (2016); (15) Plavchan et al. (2009); (16) Ramirez et al. (2012); (17) Rhee et al. (2007); (18) Vican (2012); (19) Vican (2011); (20) Weise et al. (2010); (21) Zuckerman et al. (2011); (22) Zuckerman & Song (2004).

Table 3: The amount of suitable archival spectra for RVSPY targets observed during the 1st year

Name	FEROS	Hires	HARPS
HD 377	5	65	...
HD 1466	9	...	24
HD 1835	9	...	9
HD 3296
HD 3670
HD 5133	3
HD 5349	8
HD 7570	2	...	63
HIP 6276	23
HD 10008	2	14	19
HD 13246	1
HD 14082B
HD 15060
HD 16673
HD 17925	4	...	48
HD 19668	1	17	23
HD 22484	7
HD 23356	...	77	33
HD 23484 6	1
HD 33081	8
SAO 150676	4
HD 38397	23
HD 38949	11	15	...
HD 40136	2	...	36
HD 43989	19
HD 48370	1
HD 50571	2
HD 53143	3	...	25
HD 57703
HD 59659	1
HD 59967	1	...	47
HD 72687	2
HD 76151	9	...	7
HD 76748
HD 76653	5	...	44
CD -49 3972
HD 84075	1	...	12
HD 90905	...	13	24
HD 92945	2	...	39
HD 93932	4	...	10
HD 101259	...	30	...
HD 104231
HD 107146	4	18	...
HD 107649
HD 108857
HD 109832	1
HD 111520
HD 111631	...	50	10
HD 114082	3
HD 115820	5
MML 36	9
HD 118972	2
HD 122948
HD 131156
HD 139664	1	...	8
HD 141011
HD 141521	4
HD 143811
HD 145560
HD 145972	3

Continued on next page

Table 3 – Continued from previous page

Name	FEROS	HIERES	HARPS
HD 166348	21
HD 181327	9	...	64
HD 191089	3	9	30
HD 191849	2	...	39
HD 199260	5	...	51
CPD-72 2713	14
HD 218340
HD 218511	3
HD 219482	6	...	34
HD 223340	15